1D Model Estimation of Free Surface Location in a Polymer Fiber Drawing Process

Lakshmi Narasimha Murthy Doddasomayajula

A thesis
submitted in partial fulfillment of the
requirements for the degree of

Master of Science in Mechanical Engineering

University of Washington
2019

Committee:
James Riley
Dana Dabiri

Program Authorized to Offer Degree:

Mechanical Engineering

University of Washington

Abstract

1D Model Estimation of Free Surface Location in a Polymer Fiber Drawing Process

Lakshmi Narasimha Murthy Doddasomayajula

A radially lumped and axially differential control volume is used to numerically estimate free surface location in a polymer fiber drawing process. The simplified model will include the effects of temperature dependent viscosity of the polymer μ(z), variable furnace wall temperature profile Tw(z), and radiation heat transfer. Empirical relations were used to model the convective heat transfer to the polymer from the adjacent air and enclosure analysis is used to calculate radiation heat transfer between the furnace and the polymer. While the free surface shape does show a considerable error when compared to the two-dimensional simulation and experimental results from the literature, using the free surface shape and temperature profile obtained from the simplified model as an initial guess for the full three-dimensional simulations can significantly reduce convergence times.

Table of Contents

Chapter 1 : **Introduction**

Polymer optical fibers are traditionally used for the transmission of the light in medical instruments and for automotive and industrial lighting purposes. The losses in the optical transmission are of two types intrinsic losses and extrinsic losses. While intrinsic losses are due to the material, extrinsic loses arise due to defects in manufacturing processes and material impurities. The quality of the optical signal depends on the uniformity of the fiber diameter. The focus of this thesis is to develop a steady-state one-dimensional model for the polymer preform as it necks down to fiber in a heated furnace. The simplified model will include the effects of temperature-dependent viscosity of the polymer $\mu(z)$, variable heat transfer coefficient $h(z)$ associated with the adjacent gas flow, variable furnace wall temperature profile $Tw(z)$, and radiation heat transfer from the furnace walls.

Chapter One outlines the fundamentals of optical fiber manufacturing, optical losses that can result due to the manufacturing process, and finally, the motivation for a steady-state one-dimensional model. Chapter Two provides an overview of previous research in the field of fiber manufacturing. Chapter Three presents the development of governing equations and boundary conditions used in the model. The numerical scheme is outlined in Chapter Four. Chapter Five compares the numerical predictions to the experimental results from the literature, discussion and a sensitivity analysis. Finally, closing remarks are made in Chapter Six.

POF Manufacturing

Polymer optical fibers are usually manufactured in two different ways: simultaneous co-extrusion of the cladding and core, or drawing a prefabricated preform into a fiber. During co-extrusion, the optical graded refractive index profile is obtained by the diffusion of the core and cladding within the die barrel, upstream of the die exit. Once extruded, the polymer reduces

in diameter due to an applied tensile drawing force and necks down to the final fiber diameter while losing heat to the environment.

In the second method, a prefabricated preform is fed into a high-temperature furnace and drawn into an optical fiber. As the preform enters the furnace, its temperature increases due to the combination of convective and radiative heat transfer from the furnace. The preform begins to neck-down under its own weight, and cut at its thinnest point when sufficiently heated (about 150 ^{0}C for PMMA) shown in **figure 1.1**. The neck down region occurs closest to the location of the peak furnace wall temperature. The increase in the temperature of the polymer directly affects the viscosity of the polymer. The reduced viscosity and the weight of the material are responsible for the polymer to extend past the neck down region.

At the inlet, the preform is fed through the top iris using a stepper motor to maintain a constant feed velocity shown in **figure 1.2**. The diameter of fiber exiting through the bottom iris is not actively controlled, but a pinch wheel is used to control the draw speed. A laser diameter gauge is used to measure the diameter at the exit in real-time. The furnace temperature is manipulated by active control of peak wall temperature.

The accurate prediction of draw force is important because, if the draw force is too high, the ultimate tensile strength of the polymer might be exceeded and the fiber may break. A high draw force can also result in residual stresses which can affect thermal stability of the drawn fiber. If the draw force is too low, the fiber might glob up causing detrimental variations to the fiber diameter. The draw force is primarily a function of viscosity which is temperature dependent, so accurate prediction of draw force requires a detailed analysis of heat transfer within the furnace. The heat transfer in turn depends on the viscosity and draw force this making it a highly coupled problem.

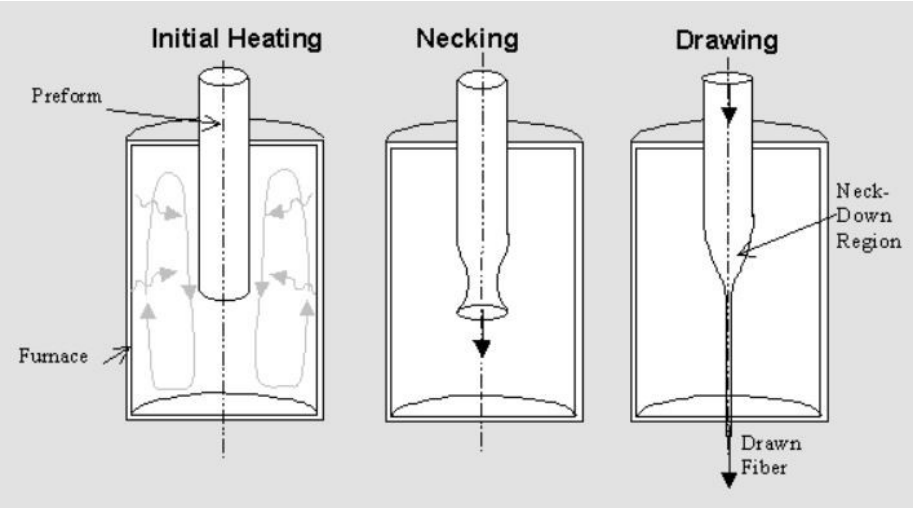

Figure 1.1: The neck down region during the polymer fiber drawing[28]

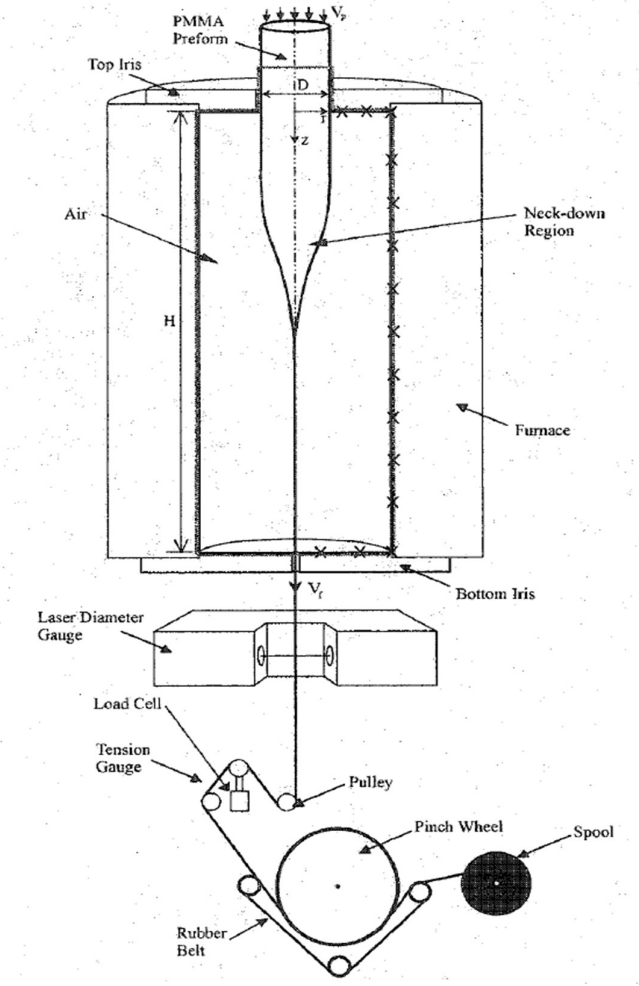

Figure 1.2: Drawing process of polymer fiber from a preform[17]

Motivation

Non-uniformity of the fiber diameter can cause micro-bend losses of the signal. Diameter variations are caused by factors such as material defects, and preform diameter irregularities. More importantly, the oscillations in the gas phase typically leads to non-uniformity of the diameter. In the previous research, the oscillations are always observed to be 3-D. A 3-D simulation typically takes a significant computational resources. A steady-state 1-D modelling of the polymer as it is being drawn can be used to estimate the free surface location of the polymer. The polymer's estimated free surface position from the simplified model can then be used as an initial guess for full three-dimensional simulations with the goal of reduced convergence times.

Chapter 2 : **Literature review**

Polymer optical fiber drawing has received relatively little attention in contrast with glass fiber drawing and melt spinning of fiber. The physics involved in glass drawing and melt spinning are similar to the drawing of polymer optical fiber; therefore, literature in glass drawing and melt spinning will be reviewed in this chapter first. Later, we will look at polymer melt spinning studies and the steady-state polymer drawing.

Glass fiber studies

One-dimensional studies

One of the earliest investigations on the dynamics of glass melting was studied by Glicksman[1] using a number of simplifying assumptions such as the small slope approximation for the radius and negligible variation of velocity and temperature across the cross-section of the jet. The most important contribution of the study is the development of one-dimensional momentum equation for the circular cross-section of the jet.

Following the work of Glicksman[1] on viscous jets, Paek and Runk[2] developed a physical model to predict the temperature distribution and the neck-down shape during the drawing of 1.2 cm diameter fused silica rods. Since the Biot number was found to be the less than 0.1, the model is reduced to a one-dimensional problem with an axial variation of heat flux. The model also neglects the inertial terms in the force balance, since the Reynolds number of the flow fields was found to be small. The force balance utilized by the authors also assumed inelastic, elongational flow and accounted only for the rheological force. The energy equation was modeled by including the axial conduction along with the glass and the radiation heat transfer. The temperature before and after the neck-down region is used as the boundary conditions for the energy equations. The free surface is predicted by iteratively solving the momentum and

energy equations. The model developed by the authors demonstrated good agreement with experimental values.

The seminal work by Peak and Runk[2] was followed by Vasili et al[3], where the authors numerically studied the neck down region accounting for the Trouton viscosity model, surface tension, inertial forces, drag forces, and gravity in the momentum balance. The model assumed that the velocity and temperature of the glass are only functions of axial coordinate. The energy equations included the effects of radiation, conduction, mixed convection (free and forced), and viscous dissipation on the neck-down region, with a known temperature at the inlet and zero heat loss at the exit. Viscous dissipation was found to have a negligible effect on the temperature distribution. Tension is influenced by gravity, surface tension and viscous forces in the upper area, and only by viscous forces in the lower area. The mathematical model, when compared with experimental data, showed a good agreement.

Extensional/Elongational model

The extensional model is used by many authors[2, 3, 8] to predict the normal viscous stress acting on the polymer. Extensional rheology focuses on pulling on a piece of material in a purely extensional manner, i.e. no shear. In an extensional flow, a rubber band will continue to elongate until you cannot stretch it any further. The first use of extensional viscosity, under a different name (coefficient of viscous traction), is that by Trouton. The ratio of extensional viscosity to the shear viscosity is called Trouton ratio. For a Newtonian fluid, the Trouton ratio is 3. So the relation between the extensional stress to strain rate is given by the equation 2.1.

$$\sigma_{zz} = 3\mu \frac{du}{dz} \tag{2.1}$$

Here σ_{zz} is the normal stress along z, and u is the velocity of the fluid along z.

Two-dimensional studies

The widespread adoption of glass fiber increased the need for a more advanced model to increase the quality of the fiber produced. The heat transfer within the furnace and preform was extensively studied by Lee and Jaluria[4, 5, 6, 7]. By starting with the free surface shape given by Paek and Runk[2], Lee and Jaluria[4] studied the effects of the necking shape and furnace temperature profile on the radiative exchange during fiber drawing. The authors applied a net enclosure method to model the exchange between the preform/fiber surface and the furnace walls and showed that a radiative coupling existed between the preform geometry and the furnace, which had been ignored by previous investigators. It was found that as the diameter of the preform/fiber decreases, the heat flux absorbed by the preform increases due to the increased self-viewing of the furnace. Lee and Jaluria[5] investigated the effects of variable properties and viscous dissipation on the temperature profile. They showed that while the viscous dissipation is small relative to the furnace heating, it significantly impacts the exit temperature due to localization to a small volume near the fiber region.

Roy Choudhury et al[8], in a detailed study of the glass flow, modelled the neck down profile on the basis of a vertical momentum and surface force balance. A radial lumping of axial velocity was used to develop a robust numerical scheme to generate the neck down the profile. They also studied the effects of the operating parameters on the neck down region. They found that for a given heat transfer coefficient at the surface, if the furnace temperature is not high enough, the fiber cannot be drawn at any arbitrary velocity. Numerically, if the furnace temperature is not high enough, the glass profile becomes flat at a certain downstream location ($\frac{dr}{dz} = 0$), and since the fiber drawing velocity and fiber diameter are fixed, this results in an abrupt change in radius of the fiber at the lower end of the furnace. In real-life fiber drawing, if the temperature level drops below the softening point, the fiber breaks because of the high viscosity of the material. This phenomenon is referred to as viscous rupture. Thus, for a given furnace

temperature and heat transfer coefficient, there exists a minimum fiber diameter that can be drawn. The neck-down profile was also found to depend on the length of the heating zone, furnace radius, and thermal conditions applied at the top of the preform. The numerical results obtained by the authors agree very well with experimental data on the neck-down profile.

Papamicheal et al[9] developed a numerical model to analyse the heating zone in optical fiber drawing. They also conducted a detailed numerical and experimental study of natural convection through an open furnace. Numerical calculations were conducted using PHOENICS. Experimentally, the high temperature of the furnace necessitated the use of water as the working fluid. While the authors did not report any time-varying flow behaviour, they appreciated that gas-phase perturbations in the furnace affected the diameter uniformity.

Melt spinning studies

The major difference in the physics of glass drawing and polymer fiber drawing is the effect of radiation. In glass drawing the furnace is heated to a temperature of 2200 ^{0}C, where radiation is the dominant form of heat transfer. In contrast, polymer drawing (especially PMMA) is performed at a maximum temperature of around 180 ^{0}C where the effect of radiation and convective heat transfer are of the same order.

Early studies on polymer fiber were focused on the melt spinning of the polymer. In the process of melt spinning shown in **figure 2.1**, a polymer is melted and heated to a suitable viscosity for fiber production. The melted polymer is pushed through a spinneret, which is a type of die consisting of several small holes. Each hole produces an individual fiber, and the number of holes on a spinneret defines the number of fibers in the yarn. The melted polymer fibers then pass through a cooling region and the fibers are combined to form a yarn and a spin finish is applied.

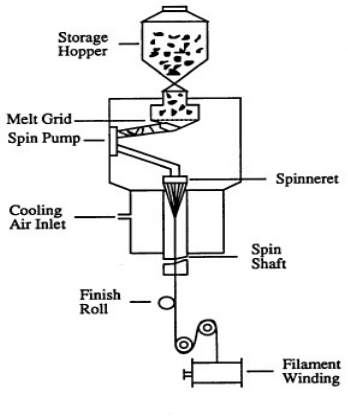

Figure 2.1: Melt Spinning of polymer[29]

The dynamics of melt spinning were extensively studied by Kase and Matsuo[10, 11] using a set of fundamental equations. The authors utilized the assumptions of radially lumped temperature, negligible axial conduction, and negligible air resistance. To allow for analytical solutions of the equations, they ignored both gravity and inertial terms. Steady state results are obtained for the temperature profile, draw tension and cross-sectional area of the polymer which show fairly good correlation with experimental results. One of the most seminal contributions of the study was experimental determination of heat transfer coefficient of coaxial air flow past a cylinder (equation 2.2). The heat transfer coefficient thus obtained is used to study the heat transfer during the melt spinning of the polymer. The author's predictions include the increase in polymer solidification distance with increase in polymer flow rate. Lowering of air temperature or increasing the cooling air speed will increase the tension and result in a thinner filament. An increase in spinneret temperature, decreases the filament tension.

$$\mathrm{Nu}_D = 0.42\mathrm{Re}_D^{0.334} \tag{2.2}$$

Here Nu_D and Re_D are the Nusselt number and Reynolds number based on the diameter of the cross-section.

Kase[12] analyzed the velocity field inside the molten spinning thread numerically by solving the continuity and momentum under several simplifying conditions. Under most conceivable spinning conditions, for a viscosity profile given in equation 2.3, the velocity profile was found to be flat across the cross- section of the fiber. Nakamura et al[13] found that for industrial spinning conditions, the effect of temperature dependent properties like density and specific heat of the polymer was found to be small on the free surface shape. Chung and Iyer[14] extended the earlier work of Kase and Matsuo[11] by including internal thermal resistance of the fiber and the external radiative effects for steady state operating conditions. Numerical results obtained by the authors show that, there is a significant variation in the radial temperature between the center and the surface of the fiber. The deviation from the Kase and Matsuo[10] is observed due high Biot numbers studied here.

$$\mu = \mu_0 e^{\beta z}(1 + cr^2) \tag{2.3}$$

Here μ is the viscosity of the polymer, and μ_0, β, and c are constants.

Studies on POF drawing

The manufacturing costs of polymer optical drawing can be reduced by reaching the steady state drawing conditions rapidly. The effect of wall temperature profile on the transient heating of preform was studied by Reeve et al[15] .The axisymmetric system modelled in the study consisted of polymer preform and the surrounding air, the preform was heated due to natural convection and radiation inside the furnace. No slip condition was applied on all the surfaces of enclosures. The preform extends from halfway into the furnace to 5cm above the top enclosure of the furnace.

The initial reduction in viscosity and necking occurs near the high temperature region of the furnace and where there was enough weight of polymer below. A parabolic temperature profile

with a peak temperature 180 ^{0}C was applied on the furnace walls. The authors considered three cases as shown in **figure 2.2**, with peak wall temperatures at 0.2m, 0.1m, and 0.3m from the base of the furnace, to study the effects of vertical translation of peak wall temperature on transient heating. The conservation equations were computationally solved using the SIMPLER finite element algorithm for both polymer and the air. For a steady state drawing, the optimum temperature profile was found be case 1.

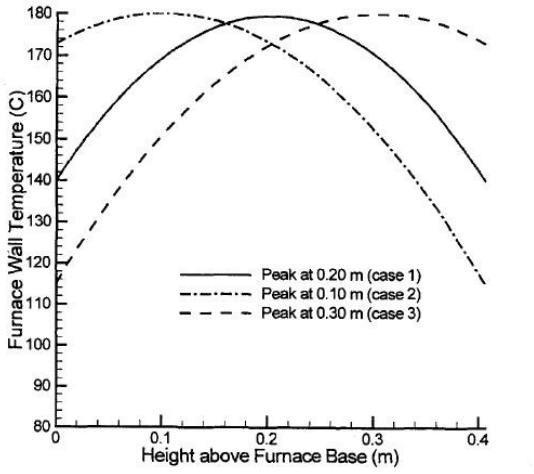

Figure 2.2: Furnace wall temperature profiles[15]

The authors also reported the relative contribution of thermal radiation and natural convection on the initial heating of the preform. The overall trend showed a decrease in combined thermal radiation and natural convection heat rates as the temperature difference between the preform and the furnace decreases. It is reported that for a 0.5in PMMA preform, the maximum heat transfer occurred 12 seconds after the insertion of the cold rod. This was the time required for establishing a natural convection cell, as at the same time the air circulation was found to be maximum with a peak velocity of 0.53 m/sec. After 12 seconds, they found that the contribution of convection decreased from 50% to 25% of total heating. This was observed because the 'effective' heat transfer coefficient of radiation increases with increasing preform temperature.

The contribution of radiation heat transfer with increasing polymer temperature is shown in **figure 2.3**.

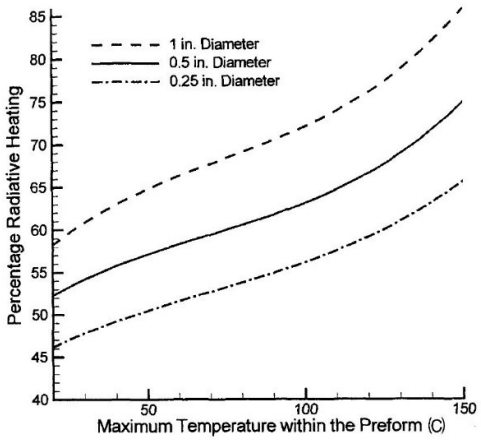

Figure 2.3: Percentage of heating due to thermal radiation with preform temperature for different preform diameters[15]

Figure 2.3 also shows that the contribution of radiation increases with increasing preform diameter. The authors explained that while both the convective and radiative heat transfer rates decrease with increase in the diameter of the preform, the contribution of convection decreases more rapidly than that of radiation due to weakening of the convective cell with an increasing preform diameter.

Reeve et al[16] conducted a steady-state two-dimensional numerical study of the gas phase and polymer during the drawing process. The authors solved two-dimensional axisymmetric conservation equations for both the air and the polymer. The polymer shear rate was found to be small, so the shear force on the polymer by the air is neglected. The boundary conditions included feed speed and infinite fin at the top and draw speed at the end for the furnace. Using the experimentally measured polymer's zero-shear viscosity as shown in **figure 2.4**, the author's obtained a best fit equation measured to numerically model the temperature dependent viscosity (equation 2.4). The authors used an enclosure method to calculate thermal radiative heat flux experienced by the polymer. The furnace enclosure and polymer were assumed to be optically thick grey surfaces.

For T >109 ^{0}C $\mu = 1.506 \text{ X } 10^5 \exp(2935 \left(\frac{1}{T} - \frac{1}{170\ ^0C}\right))$ N/m^2 (2.4)

For T <109 ^{0}C $\mu = 2.3 \text{ X} 10^9$ N/m^2

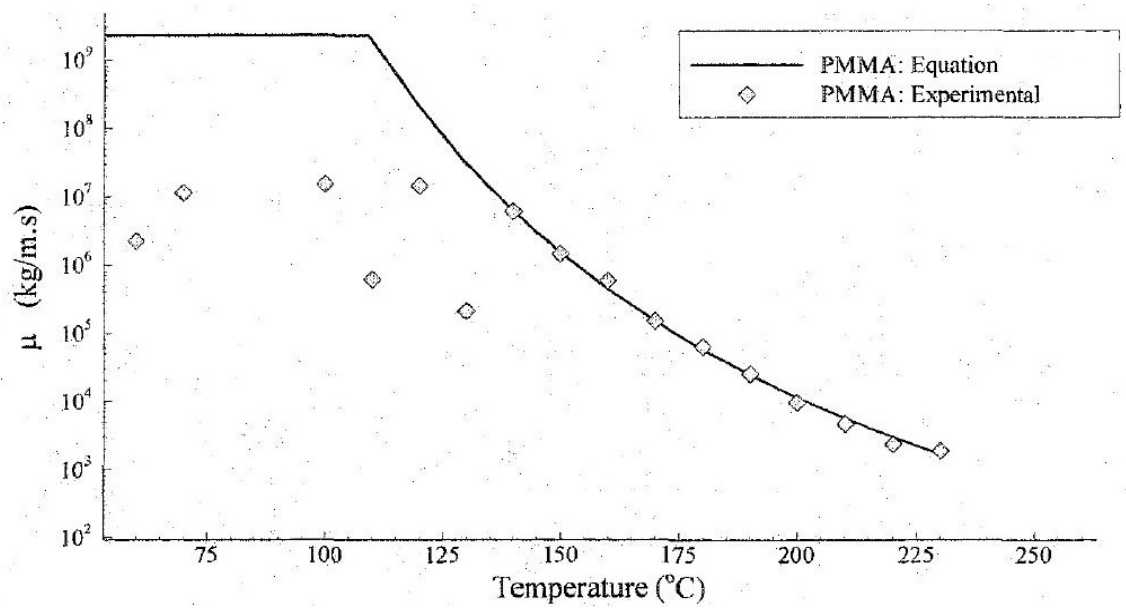

Figure 2.4: Temperature dependence of zero-shear viscosity[17]

The numerical investigation was conducted on four cases with varying feed speed, draw speed preform radius, and peak wall temperature. A commercial finite element code FIDAP was used to solve the velocity and temperature fields. The numerical results from the study predicted that thermal radiation accounts for 70% of the polymer's heating but only 15% of the polymer's cooling. These results here agree with the transient heating study of Reeve et al[15] and the melt spinning study of Chung and Iyer[14]. The heat flux predicted by the numerical study is found be in good agreement with empirical relation by Kase and Matsuo[14]. The authors found that the draw force is highly dependent on both the polymer feed rate and the furnace wall temperature. A change of 1°C in polymer temperature can result in a 10% change in the draw force. The

study found that, due to the low feed rates and low processing temperatures of polymer optical fiber drawing, the effect of upstream heating on the free surface shape cannot be ignored.

Effect of natural convection on the exit fiber diameter

Because the natural convection plays a significant role in the heating and cooling of the polymer, the exit diameter of the fiber is strongly influenced by natural convection. Reeve[17] performed experiments on the effects of unsteady natural convection during a polymer fiber drawing process. Starting with the steady-state drawing of a preform with 0.025 m diameter, Reeve decreased the temperature of the top iris (increasing buoyant potential) from 115.5 ^{0}C to 104.8 ^{0}C. The convective flow was observed to transition from laminar to oscillatory and then finally to chaotic flow. Reeve found that the time-varying temperature in the oscillatory flow regimes and chaotic flow can have detrimental effects on the fiber diameter as shown in **figures 2.5** and **2.6**.

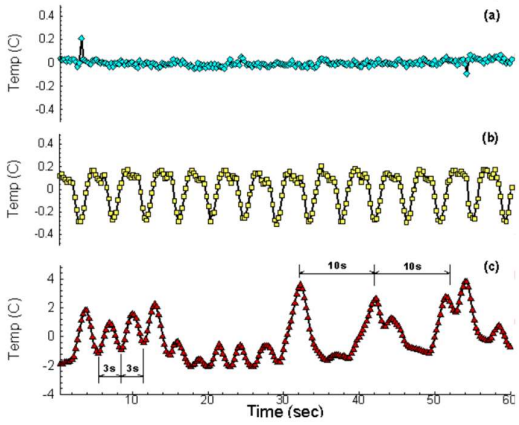

Figure 2.5: Air temperature history from sample mean (a) Laminar (b) Oscillatory (c) Chaotic flow regimes(Note different scales on y-axis) [17]

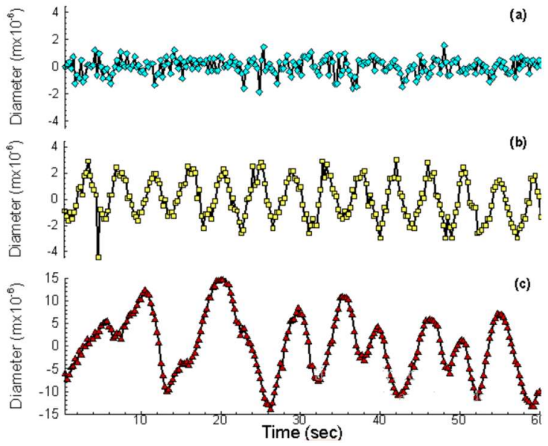

Figure 2.6: Exit diameter history from sample mean for corresponding air temperatures in figure 2.5(a) Laminar (b) Oscillatory(c) Chaotic flow regimes (Note different scales on y-axis) [17].

The author observed that while the fiber drawn under oscillatory regime showed cyclic diameter variations, the chaotic air temperature led to even more dramatic diameter variations. The standard deviation of diameter in oscillatory and chaotic regimes was found be about 2.5 and 10 times greater, respectively than that of the laminar regime.

The author also studied the effect of preform diameter on the fiber diameter variations by conducting experiments on preform with a diameter of 0.038m. While the final diameter and furnace temperature remain unchanged, the feed speed was decreased to keep mass flow rate constant. The experiments indicated that, while the oscillatory flow regime started at similar temperature conditions, the chaotic flow does not start even when the top iris was cooled to 50 ^{0}C. The author suspected that the nature of the oscillating regime is dependent on the Rayleigh number at the necking zone, while nature of the chaotic regime is dependent on the Rayleigh number at the entrance. The Rayleigh number at the necking zone is almost same for the drawing of both the radii, while the Rayleigh number at the entrance is smaller for the case of the preform with high diameter. This is why, while the oscillatory regime starts at similar iris temperature, the chaotic regime is does not start even if the iris temperature is decreased to 50 ^{0}C.

Chapter 3 : **Physical Model**

The numerical model used to study the polymer fiber drawing is a steady-state, quasi-one-dimensional model. This chapter presents the governing equations for the fiber draw process, followed by the discussion on the modeling of radiation heat transfer, empirical relations for the convective heat transfer. Finally at the end of the chapter, boundary conditions for the numerical model are presented.

The polymer enters the domain with a preform diameter (D) and a constant feed velocity (w_0). The preform necks down while passing through the furnace due to the natural convection, radiation heat transfer from the furnace and applied draw force. The assumptions used for the model are as follows:

1. Negligible change in velocity and temperature along the radial coordinate of the polymer.
2. Constant polymer density, thermal conductivity, and specific heat.
3. Negligible shear stress on the polymer.
4. Steady, but spatially variable total heat transfer coefficient h(z) (heat transfer coefficient from free and forced convection, and effective heat transfer coefficient of radiation).

The most important of these assumptions is the quasi-one-dimensional assumption, which assumes that the velocity and temperature are independent of r and theta. This assumption decreases the complexity of the model, and the computational resources required for the solution. It is necessary that the velocity component and the temperature changes along the radial direction be small for this assumption to be valid.

Governing equations

The equations governing the flow of the polymer are the conservation of mass, momentum/force balance, and conservation of energy. The polymer is considered to be an incompressible fluid with temperature-dependent viscosity. The conservation equations were applied to the control volume shown in **figure 3.1**, which is lumped across the cross-section and differential along the axial direction.

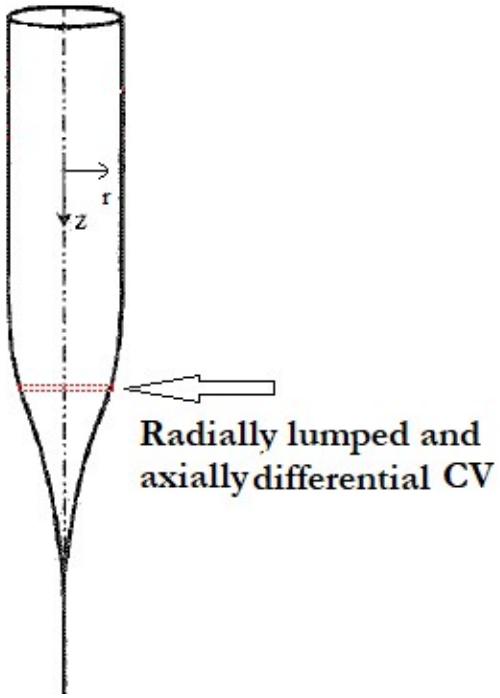

Figure 3.1: Control volume of the polymer element

Applying the mass conservation on the control volume,

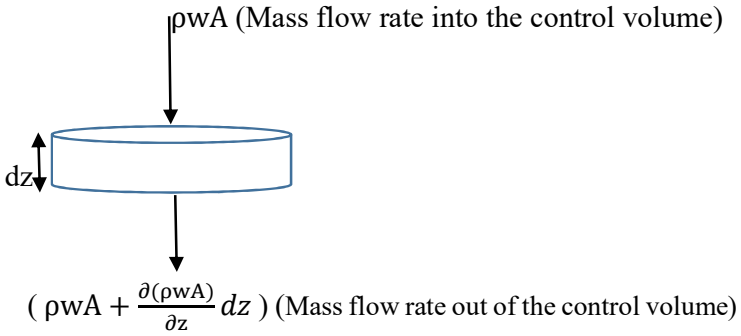

$$Mass\ flow\ into\ the\ CV - Mass\ flow\ out\ of\ the\ CV = \ Rate\ of\ change\ of\ mass\ inside\ the\ CV$$

$$\rho wA - \rho wA - \frac{\partial(\rho wA)}{\partial z}dz = \frac{\partial(\rho Adz)}{\partial t}$$

$$\frac{\partial(\rho wR^2\pi)}{\partial z} = -\frac{\partial(\rho R^2\pi)}{\partial t}$$

Since the polymer flow is assumed to be incompressible and steady state,

$$wR^2 = \text{constant}$$

$$\mathbf{wR^2 = w_0 R_0^2} \qquad (3.1)$$

Here z is the axial coordinate, ρ is the density of the polymer, A is the cross-sectional area of the control volume, R is the radius of the polymer element, w is the velocity of the polymer element, w_0 is the feed velocity of the preform, and R_0 is the radius of the preform.

The body force acting the control volume is the gravity, and the surface force acting on the control volume is the normal stress.

Applying force/momentum balance on the control volume,

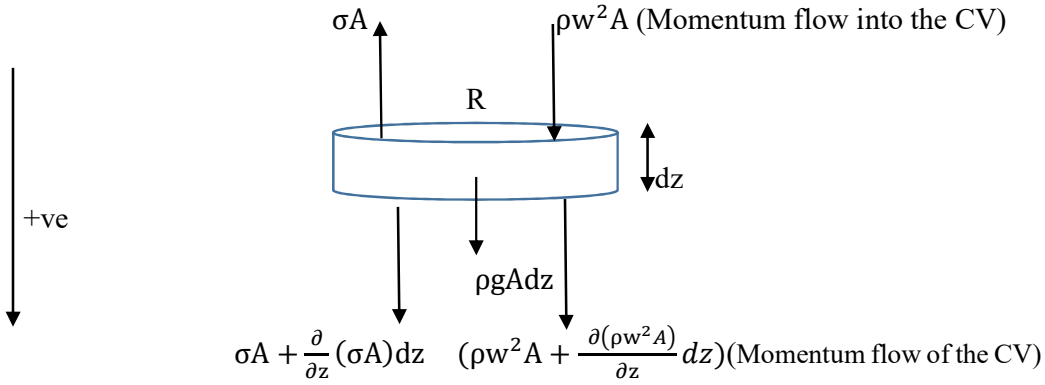

$$\sum F_z = Momentum\ flow\ out\ along\ z - Momentum\ flow\ in\ along\ z$$

$$+ Change\ in\ momentum\ with\ time$$

$$\rho gAdz + \frac{\partial}{\partial z}(\sigma A)dz + \sigma A - \sigma A = \rho w^2 A + \frac{\partial(\rho w^2 A)}{\partial z}dz - \rho w^2 A + \frac{\partial(\rho wAdz)}{\partial t}$$

$$\rho gA + \frac{\partial}{\partial z}(\sigma A) = \frac{\partial(\rho wA)}{\partial t} + \frac{\partial(\rho w^2 A)}{\partial z}$$

$$\rho gR^2\pi + \frac{d}{dz}(\sigma R^2\pi) = \rho wR^2\pi\frac{dw}{dz}$$

An extensional flow model is used to model the normal viscous stress,

$$\sigma = 3\mu\frac{dw}{dz}$$

$$\rho w R^2\pi\frac{dw}{dz} = \rho g R^2\pi + \frac{d}{dz}\left(3\mu\frac{\partial w}{\partial z}R^2\pi\right)$$

$$\mathbf{w\frac{dw}{dz} = g + 3w\frac{d}{dz}\left(\frac{\mu}{w\rho}\frac{dw}{dz}\right)} \quad (3.2)$$

Finally, applying conservation of energy on the control volume,

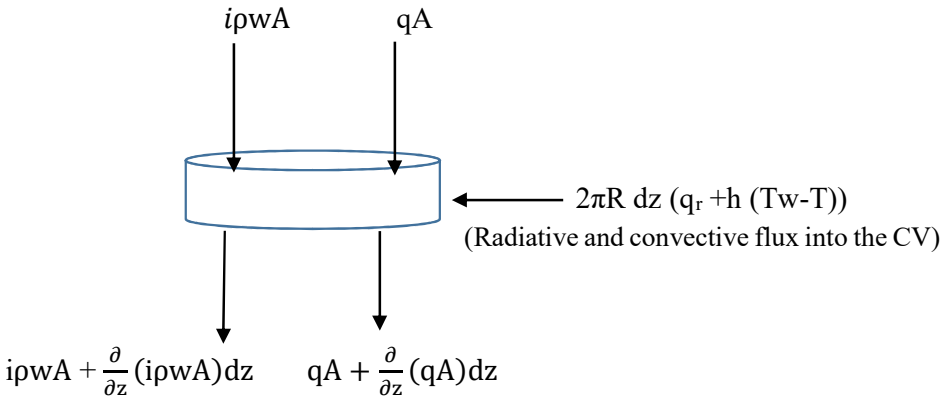

Energy into the CV - Energy out of the CV = Change of energy within the CV with time

$$\left(i\rho wA - i\rho wA - \frac{\partial(i\rho wA)}{\partial z}dz\right) + (qA - qA - \frac{\partial}{\partial z}(qA)dz) + 2h(Tw - T)R\pi dz + 2\pi R\, q_r dz$$

$$= \frac{\partial(i\rho wAdz)}{\partial t}$$

$$i = cT$$

$$q = -k\frac{\partial T}{\partial z}$$

$$2h(Tw - T)R\pi + \frac{\partial}{\partial z}\left(k\frac{\partial T}{\partial z}R^2\pi\right) + 2\pi R\, q_r - \frac{\partial(i\rho wA)}{\partial z} = \frac{\partial(i\rho A)}{\partial t}$$

$$\frac{d(\rho w R^2 cT\pi)}{dz} = 2h(Tw - T)R\pi + \frac{d}{dz}\left(k\frac{dT}{dz}R^2\pi\right) + 2\pi R\, q_r$$

$$\frac{\mathbf{dT}}{\mathbf{dz}} = \frac{\mathbf{2h}}{\mathbf{\rho cRw}}(\mathbf{Tw} - \mathbf{T}) + \frac{\mathbf{k}}{\mathbf{\rho c}}\frac{\mathbf{d}}{\mathbf{dz}}\left(\frac{\mathbf{1}}{\mathbf{w}}\frac{\mathbf{dT}}{\mathbf{dz}}\right) + \frac{\mathbf{2}q_r}{\mathbf{\rho cRw}} \quad (3.3)$$

Here T is the temperature of the polymer, C is the specific heat of the polymer, k is the thermal conductivity of the polymer, Tw is the furnace temperature and h is the effective heat transfer coefficient. The temperature dependent viscosity is modeled using equation 2.4.

Radiation Modelling

Radiative heat transfer occurs exclusively through the surface to surface exchange and is usually treated using an enclosure analysis. In the enclosure analysis of non-isothermal concentric cylinders, we consider the radiation heat transfer on a single polymer element from all the surrounding wall elements. The view factor from the furnace elements to a polymer element is taken from Reid and Tennet[29] when the elements are coaxial and Leuenberger and Person[30] for the case of concentric elements. The net heat transfer rate between two radiation elements forming an enclosure is given by equation 3.4.

$$Q_{i\to j} = \frac{\sigma((T_i+273)^4 - (T_j+273)^4)}{(\frac{1-\varepsilon_w}{A_i\varepsilon_w} + \frac{1}{A_iF_{ij}} + \frac{1-\varepsilon_p}{A_j\varepsilon_p})} \quad (3.4)$$

Here σ is the Stefan-Boltzmann constant, 'i' is the wall element, 'j' is the polymer element, F_{ij} is the view factor from wall element 'i' to polymer element 'j' ε_w is the emissivity of wall, ε_p is the emissivity of polymer, A_i is the area of the furnace wall element, and A_j is the area of the polymer.

The total heat flux gained or lost by the each polymer element is given equation 3.5.

$$q_j = \frac{1}{A_j}\sum_{i=1}^{n} Q_{i\to j} \quad (3.5)$$

Empirical Relations for the heat transfer coefficient

This objective of this study is modelling the polymer during the polymer optical fiber drawing. The convection from the adjacent air inside the furnace plays a major role in heating and cooling of the polymer. So, empirical relations were used to model the heat transfer from the air.

Free convection heat transfer coefficient

Literature from natural convection over a vertical cylinder are reviewed here. Free convective heat transfer from vertical slender cylinders and a flat vertical plate can differ significantly because of the transversal curvature effect, especially when the thermal boundary layer thickness δT is comparable or thicker than the radius of cylinder (i.e., where transverse curvature influences boundary layer development and increases the rate of heat transfer). Using the perturbation method, Fuji and Uehara[18] calculated the heat transfer coefficient of laminar natural convection on a vertical cylinder for fluid in the Prandtl number range of 0.72-100. They provided empirical relations under for boundary conditions of temperature (equation 3.6(a)) and heat flux distribution (equation 3.6(b)) as a function of the vertical distance. Ramachandran et al[19] used numerical methods to obtain an expression for Nusselt number in terms of Rayleigh number for a vertical cylinder in a quiescent bulk fluid (equation 3.7). The numerical results were found to be in good agreement with previous experimental work by the authors[20].

For the case of $q_w = Mx^n$

$$\mathrm{Nu_x} = \mathrm{Nu_{x,Fp}} + 0.345\frac{\mathrm{x}}{\mathrm{r}} \qquad (3.6(a))$$

For the case of $T_w - T_a = Nx^n$

$$Nu_x = Nu_{x,Fp} + 0.435\frac{x}{r} \quad (3.6(b))$$

Here $Nu_{x,Fp}$ is the Nusselt number of laminar natural convection over a vertical flat plate and Nu_x is the Nusselt number of laminar convection based on x and r is the radius of the cylinder.

$$Nu_D = 0.55Ra_D^{0.20} \quad (3.7)$$

Here Ra_D is the Rayleigh number based on the cylinder diameter D.

Kimura et al[21] experimentally studied the natural convection of water over a vertical cylinder with constant heat flux. The experimental results for a Grashof number below 3.7 X 10^9 were found to be in good agreement with the numerical results from Fuji and Uehara[18]. Cebeci[22] compared the natural convection heat transfer between the vertical flat plate and vertical cylinder and provided a criterion when the curvature significantly affects the heat transfer. The author also studied the natural convection over an isothermal vertical cylinder for the Prandtl numbers 0.72 and 6 (equation 3.8). The theoretical results of Cebeci[22] were correlated by Popiel[23].

$$\frac{Nu_x}{Nu_{x,Fp}} = 1 + 1.5[Gr_H^{-0.227}\frac{H}{D}^{0.909}] \quad (3.8)$$

Here Gr_H is the Grashof number based on the length of the cylinder H.

The empirical relations from laminar natural convection over a vertical cylinder could not completely capture the natural convection of air inside an annulus. The empirical relations from natural convection of a fluid in vertical annulus are considered. The benchmark study by Thomas and Davies[24] provide an empirical relation for the Nusselt number of fluid between two concentric isothermal cylinders. The authors numerically investigated laminar natural convection in a closed vertical annulus, with the inner surface at a higher temperature than the outer surface. The authors found that the convection is strongly dependant on Rayleigh number,

annulus width and aspect ratio. The flow inside the annulus was classified into conduction, transient and boundary layer regimes. The authors provide the criteria for conduction and boundary layer regimes for a Prandtl number of 1, and aspect ratio greater than 5 given in equations 3.9(a), 3.9(b).

For conduction regime

$$\frac{\mathrm{Ra}}{\mathrm{H}} < 400 \tag{3.9(a))}$$

For the boundary layer regime

$$\frac{\mathrm{Ra}}{\mathrm{H}} > 3000 \tag{3.9(b))}$$

Here H is the aspect ratio.

Numerically solving the conservation equation, the authors obtained Nusselt number correlations for all three of the flow regimes. Equation 3.10 gives the correlation between the Nusselt number and Rayleigh number for the conduction regime.

$$\mathrm{Nu} = 0.595\ \mathrm{Ra}^{0.101}\mathrm{Pr}^{0.024}\ \eta^{0.505}\ \mathrm{A}^{-0.052} \tag{3.10}$$

$$\mathrm{Ra} = \frac{g\beta_{air}}{\alpha_{air}\upsilon_{air}}(\mathrm{T_o} - \mathrm{T_i})\left(\mathrm{R_o} - \mathrm{R_i}\right)^3$$

$$\eta = \mathrm{R_o}/\mathrm{R_i}$$

$$\mathrm{A} = \mathrm{H}/(\mathrm{R_o} - \mathrm{R_i})$$

Here η the radius ratio.

Kumar and Kalam[32] numerically investigated the effects of diameter ratio and aspect ratio in natural convection of gases within vertical annuli. They maintained the inner cylinder at higher temperature than and the outer cylinder. They provide correlations (equation 3.11) for the radius ratio between 1 and 15 and the aspect ratio between 0.3 and 10.

$$\mathrm{Nu} = 0.18\ \mathrm{Ra}^{0.278}\ \eta^{\frac{0.329}{\eta}+0.34}\ \mathrm{A}^{-0.122} \tag{3.11}$$

Khan and Kumar[34] extended the analysis to the case of inner cylinder at uniform heat flux and the outer cylinder at constant temperature. They provide correlations (equation 3.12) for the radius ratio between 1 and 15 and the aspect ratio between 1 and 10.

$$\mathrm{Nu} = 0.158\ \mathrm{Ra}^{0.29}\ \eta^{\frac{0.303}{\eta}+0.316}\ \mathrm{A}^{-0.05} \tag{3.12}$$

Keyhani et al[33] experimentally measured the natural convection heat transfer of a fluid in the annulus of vertical concentric cylinders, with inner cylinder at constant heat flux and outer cylinder at constant temperature. For the case of 27.6 aspect ratio and radius ratio of 4.33 the authors provide empirical relation for the Nusselt number shown in equation 3.13.

$$\mathrm{Nu} = 1.0653\ \mathrm{Ra}^{0.077}\ \eta^{0.505}\ \mathrm{A}^{-0.052} \tag{3.13}$$

After examining all these equation we will use equations 3.10 and 3.13 and look at the results from each correlation to contrast their effect on the free surface radius.

Forced convection heat transfer coefficient

One of the most commonly used empirical relations for the forced convection was given by Kase and Matsuo[10] shown in equation 2.2. The authors conducted experiments with a heated stationary wire to obtain the empirical relation. Using dimensional analysis, Andrews[25] found that Nusselt number is function of Reynolds number, and the author numerically derived equation 3.14 by using empirical diameter-distance data.

$$\mathrm{Nu}_D = 0.764\mathrm{Re}_D^{0.38} \tag{3.14}$$

Seban and Bond[26] numerically studied the laminar boundary layer of an incompressible fluid of constant properties on the exterior of a cylinder with flow parallel to the cylinder axis. They adopted a solution method based on expansion in a series of functions. Numerically solving these functions, the authors obtained equation 3.15 for the Nusselt number. Tasse et al[27] investigated the momentum and thermal boundary layer along a yarn of circular cross section

in axial flow for two types of boundary conditions. The authors obtained quasi-similar solution for both a semi-infinite body and a continuous moving surface, using a finite difference scheme. Numerical analysis by the authors showed that boundary layer growth is affected by the boundary conditions, and fiber spinning inside a wind tunnel will not give quantitatively correct results. They obtained a correlation between Nusselt number and Reynolds number given by equation 3.16.

$$Nu_x = 0.295 Re_x^{0.50} \left[1 + 2.3 \frac{x}{(rRe_x)^{0.5}}\right] \quad (3.15)$$

$$Nu_D = 0.85 \left(\frac{Re_D}{Re_x^{0.5}}\right)^{0.5} \quad (3.16)$$

After considering all the empirical relations, we use equation 2.2 to estimate the forced convection heat transfer to as it was obtained using experimental data and it was used by many later researchers. The heat transfer during polymer cooling given by Reeve et al[16] was also found to be in good agreement with equation 2.2.

Boundary conditions

The numerical domain only consists of the polymer, so boundary conditions are imposed at the entrance and the exit of the polymer. The boundary conditions for the one-dimensional model are chosen based on the experimental fiber drawing system. Experimentally, a constant preform speed at the inlet and a constant draw speed at the exit are maintained. For the two thermal boundary conditions along the z-direction, the polymer preform above the furnace is treated as a moving infinite fin. At the exit, where the Peclet number is high, conduction in the fiber is negligible compared to energy advection associated with the fiber velocity; hence, at the fiber exit, $d^2T/dz^2 = 0$.

At z = 0,

$$R = R_0$$

$$w = w_0$$

$$\frac{dT}{dz} = \left(\frac{w}{2\alpha} + \sqrt{\left(\frac{w}{2\alpha}\right)^2 + \frac{2h_a}{kR}} \right) (T - T_a) \tag{3.17}$$

At z = L,

$$w = w_e$$

$$\frac{d^2T}{dz^2} = 0$$

Here α is the thermal diffusivity, h_a is the heat transfer coefficient between preform and ambient air, T_a is the temperature of the ambient air.

Chapter 4 : **Numerical Scheme**

The presence of temperature-dependent viscosity, variable heat transfer coefficient, and thermal radiation within the mathematical model presents a system of highly coupled equations. This chapter presents an iterative numerical scheme to solve the highly coupled non-linear conservation equations and criteria for the convergence of the numerical method.

The operating conditions for the polymer optical fiber manufacturing are shown in Table 4.1 and material and environmental properties are shown in Table 4.2.

Table 4.1: Operating conditions

Operating conditions	E1	E2	E3	E4
Feed velocity (μm/sec)	25	50	12.5	11
Draw speed (cm/sec)	10	20	5	10
Preform Diameter (mm)	25.4	25.4	25.4	38.1
Max Temperature (^{0}C)	168.8	189	168.8	168.8

Table 4.2: Material and Environmental properties

Density (Kg/m^3)	1195
Specific heat (J/Kg/K)	1465
Thermal conductivity (W/m K)	0.193
Heat transfer coefficient with ambient air h_∞ (W/m^{2}K)	10
Ambient air Temperature (^{0}C)	23
Furnace length L (m)	0.4065
Thermal conductivity of air (W/m K)	0.03251
Kinematic viscosity of air (m^2/sec)	1.48E-05

The temperature of the drawing furnace is experimentally measured using thermocouples at 10 axial positions. A 4th order polynomial fit is used to generate a functional relationship between the furnace temperature and axial coordinate (norm of the residual is 6.15). **Figure 4.1** shows the wall temperature profile for E1.

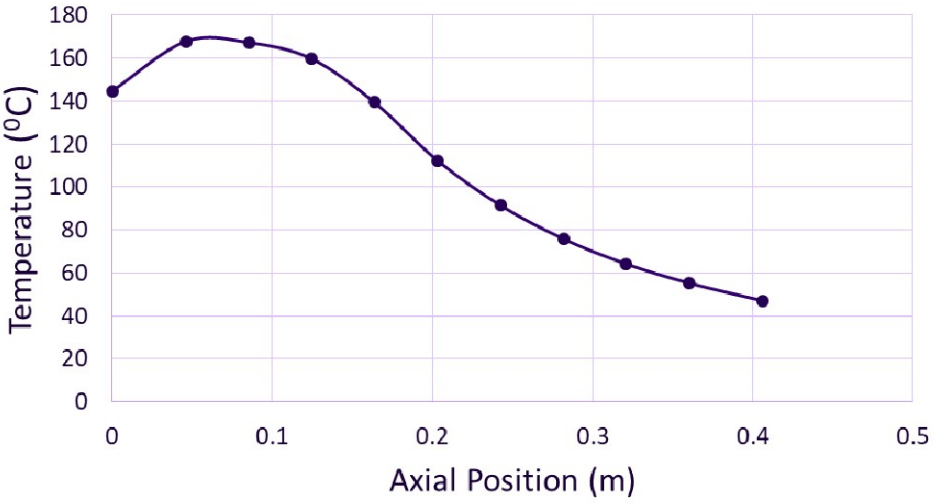

Figure 4.1: Wall temperature profile used for model predictions

The flow chart describes the iterative numerical method used to solve the coupled non-linear problem.

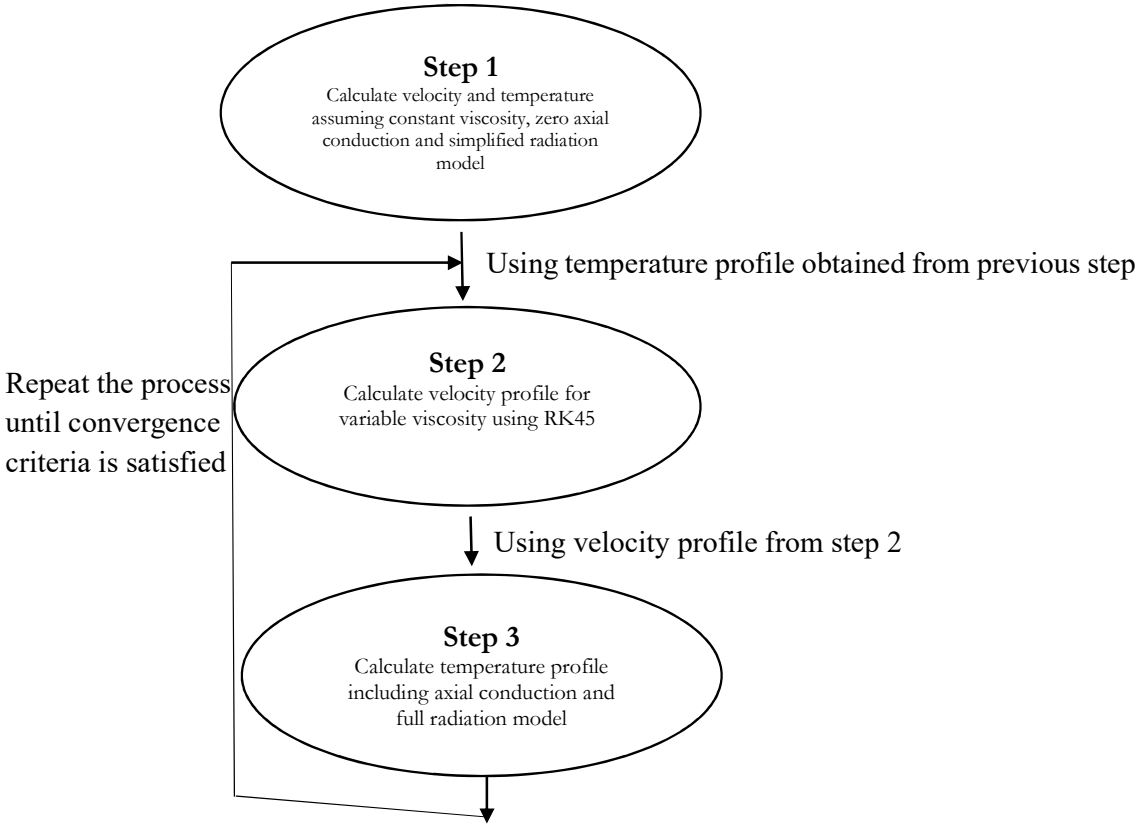

Step 1

In the first step of the numerical method the conservation equations for the case of constant viscosity and zero axial conduction are solved.

The momentum equation is used to calculate the velocity profile,

$$w\frac{dw}{dz} = g + 3w\frac{d}{dz}\left(\frac{\mu}{w\rho}\frac{dw}{dz}\right)$$

$$\frac{dw}{dz} = \frac{g}{w} + 3\frac{\mu}{\rho}\frac{d}{dz}\left(\frac{1}{w}\frac{dw}{dz}\right) \tag{4.1}$$

Integrate equation 1 w.r.t dz,

$$w = \int_0^z \frac{g}{w}dz + \frac{3\mu}{\rho w}\frac{dw}{dz} + K_1$$

Here K_1 is the constant of integration

$$\frac{dw}{dz} = \frac{\rho w}{3\mu}\int_0^z \frac{g}{w}dz + \frac{\rho w^2}{3\mu} + \frac{\rho w}{3\mu}K_1$$

Applying the finite difference equations for the velocity gradient

$$dz = z_{j+1} - z_j$$

$$\mathbf{w_{j+1} = w_j + dz\left(\frac{\rho w_j}{3\mu}\int_0^{z_j}\frac{g}{w}dz + \frac{\rho {w_j}^2}{3\mu} + \frac{\rho w_j}{3\mu}K_1\right)} \tag{4.2}$$

The subscript "j" refers to a central node, where "j+1" is the adjacent node marching forward in the numerical domain. The constant K_1 in the equation 2 is chosen such that the exit velocity is matches the draw speed of the fiber.

The temperature profile is calculated using energy equation,

$$\frac{dT}{dz} = \frac{2h}{\rho c R w}(T_{wall} - T)$$

$$\mathbf{T_{j+1} = T_j + dz\left(\frac{2h}{\rho c R_j w_j}\left(T_{wall} - T_j\right)\right)} \tag{4.3}$$

The summation of free, forced, and radiative heat transfer coefficients is used as total heat transfer coefficient h in equation 4.3. The radiation heat transfer coefficient in this step is obtained by using a simplified model. The radiation model is simplified by only considering the radiation heat transfer on the polymer element by the adjacent wall element with corresponding wall temperature. In such a model, the view factor of polymer element from the wall element is given by the ratio of areas. Equation 4.4 shows the corresponding heat transfer coefficient.

$$h = h_{Free} + h_{Forced} + h_{radiation}$$

$$h_{radiation} = \frac{\sigma((T_{wall}{}^2 + T^2)(T_{wall} + T)}{A_W\left(\frac{1-\varepsilon_w}{A_W\varepsilon_w} + \frac{1}{A_p} + \frac{1-\varepsilon_p}{A_p\varepsilon_p}\right)} \tag{4.4}$$

The temperature at z=0 is obtained by solving equations (4.5), (4.6).

$$\frac{dT}{dz} = \frac{2h}{\rho C R}\left(T_{wall} - T(z=0)\right) \tag{4.5}$$

$$\frac{dT}{dz} = \left(\frac{w}{2\alpha} + \sqrt{\left(\frac{w}{2\alpha}\right)^2 + \frac{2h_a}{kR}}\right)\left(T(z=0) - T_a\right) \tag{4.6}$$

Step 2

The temperature profile obtained from step 1 is used to calculate the velocity for the case of variable viscosity.

$$w\frac{dw}{dz} = g + 3w\frac{d}{dz}\left(\frac{\mu}{w\rho}\frac{dw}{dz}\right)$$

$$w\frac{dw}{dz} = g + \frac{3\mu}{\rho}\frac{d^2w}{dz^2} - \frac{3\mu}{\rho w}\left(\frac{dw}{dz}\right)^2 + 3\frac{dw}{dz}\frac{d}{dz}\left(\frac{\mu}{\rho}\right) \tag{4.7}$$

$$\frac{d\mu}{dz} = -1.506\,X\,10^5 \exp\left(2935\left(\frac{1}{T} - \frac{1}{170\ ^0C}\right)\right) X \frac{2935}{T^2}\ X\ \frac{dT}{dz}$$

$$\frac{d\mu}{dz} = \frac{2935\ \mu}{T^2}\frac{dT}{dz} \tag{4.8}$$

Using equations 4.7, 4.8

$$w\frac{dw}{dz} = g + \frac{3\mu}{\rho}\frac{d^2w}{dz^2} - \frac{3\mu}{\rho w}\left(\frac{dw}{dz}\right)^2 + 3\frac{dw}{dz}\left(\frac{2935\ \mu}{\rho T^2}\right)\left(\frac{dT}{dz}\right)$$

For polymer temperature below 109 ^{0}C,

$$\frac{d}{dz}\begin{bmatrix} w \\ w' \end{bmatrix} = \begin{bmatrix} \frac{dw}{dz} \\ \frac{w\frac{dw}{dz}}{3\mu} + \frac{\left(\frac{dw}{dz}\right)^2}{w} - \frac{g}{3\mu} \end{bmatrix} \tag{4.9}$$

For temperature above 109 ^{0}C,

$$\frac{d}{dz}\begin{bmatrix} w \\ w' \end{bmatrix} = \begin{bmatrix} \frac{dw}{dz} \\ \frac{w\frac{dw}{dz}}{3\mu} + \frac{\left(\frac{dw}{dz}\right)^2}{w} + \frac{2935\frac{dw}{dz}\left(\frac{dT}{dz}\right)}{T^2} - \frac{g}{3\mu} \end{bmatrix} \tag{4.10}$$

The equations 4.7 and 4.8 are solved using a 4th order Runge-Kutta method (RK45). RK45 requires an initial value for both the velocity and gradient of the velocity. The initial value of velocity gradient is chosen such that the velocity at the exit of the fiber matches the draw speed.

Step 3

Velocity profile from the step 3 is used to calculate the temperature profile using finite difference methods. In this step, the heat transfer from the each radiating wall element to the polymer element is included.

$$\frac{dT}{dz} = \frac{2h}{\rho c R w}(Tw - T) + \frac{k}{\rho c}\frac{d}{dz}\left(\frac{1}{w}\frac{dT}{dz}\right) + \frac{2q_r}{\rho c R w}$$

$$-\frac{\mathrm{k}}{\rho \mathrm{cw}}\frac{\mathrm{d}^2\mathrm{T}}{\mathrm{dz}^2}+\frac{\mathrm{dT}}{\mathrm{dz}}\left(\left(\frac{\mathrm{k}}{\rho \mathrm{cw}^2}\frac{\mathrm{dw}}{\mathrm{dz}}\right)+1\right)=\frac{2\mathrm{h}}{\rho \mathrm{cRw}}(Tw-\mathrm{T})+\frac{2\mathrm{q}_r}{\rho \mathrm{cRw}}$$

Using 2nd order finite difference approximations for the derivatives of temperature,

$$\mathrm{T}_{\mathrm{j+1}}\left(-\frac{\mathrm{k}}{\rho \mathrm{cw}_j\mathrm{dz}^2}+\left(\frac{\mathrm{k}}{2\rho \mathrm{cw}_j{}^2\mathrm{dz}}\frac{\mathrm{dw}}{\mathrm{dz}}\right)+\frac{1}{2\mathrm{dz}}\right)+\mathrm{T}_{\mathrm{j}}\left(\frac{2\mathrm{k}}{\rho \mathrm{cw}_j\mathrm{dz}^2}+\frac{2\mathrm{h}}{\rho \mathrm{cR}_j\mathrm{w}_j}\right)-$$

$$\mathrm{T}_{\mathrm{j-1}}\left(\frac{\mathrm{k}}{\rho \mathrm{cw}_j\mathrm{dz}^2}+\left(\left(\frac{\mathrm{k}}{2\rho \mathrm{cw}_j{}^2\mathrm{dz}}\frac{\mathrm{dw}}{\mathrm{dz}}\right)+\frac{1}{2\mathrm{dz}}\right)\right)=\frac{2\mathrm{h}Tw}{\rho \mathrm{cR}_j\mathrm{w}_j}+\frac{2(q_r)_j}{\rho c\ {}_j\mathrm{w}_j} \qquad (4.12)$$

$$(\mathrm{q_r})_\mathrm{j}=\frac{1}{\mathrm{A_j}}\sum_{\mathrm{i=1}}^{\mathrm{n}}\mathrm{Q_{i\to j}}$$

$$(\mathrm{q_r})_\mathrm{j}=\frac{1}{\mathrm{A_j}}\sum_{\mathrm{i=1}}^{\mathrm{n}}\frac{\sigma((\mathrm{Tw_i}+273)^4-(\mathrm{T_j}+273)^4}{(\frac{1-\varepsilon_\mathrm{w}}{\mathrm{A_i}\varepsilon_\mathrm{w}}+\frac{1}{\mathrm{A_i}\mathrm{F_{ij}}}+\frac{1-\varepsilon_\mathrm{p}}{\mathrm{A_j}\varepsilon_\mathrm{p}})}$$

$$(\mathrm{q_r})_\mathrm{j}=\sum_{\mathrm{i=1}}^{\mathrm{n}}\mathrm{hr_{ij}}(\mathrm{Tw_i}-\mathrm{T_j})$$

$$(\mathrm{q_r})_\mathrm{j}=\left(\sum_{\mathrm{i=1}}^{\mathrm{n}}\mathrm{hr_{ij}Tw_i}\right)-\left(\sum_{\mathrm{i=1}}^{\mathrm{n}}\mathrm{hr_{ij}T_j}\right)$$

$$(\mathrm{q_r})_\mathrm{j}=\left(\sum_{\mathrm{i=1}}^{\mathrm{n}}\mathrm{hr_{ij}Tw_i}\right)-\mathrm{T_j}\left(\sum_{\mathrm{i=1}}^{\mathrm{n}}\mathrm{hr_{ij}}\right)$$

$$(\mathrm{q_r})_\mathrm{j}=\mathrm{qw_j}-\mathrm{T_j}hr_j \qquad (4.13)$$

$$\mathrm{hr_{ij}}=\frac{\sigma((\mathrm{Tw_i}+273)^2+\left(\mathrm{T_j}+273\right)^2)(\mathrm{Tw_i}+\mathrm{T_j}+273+273)}{\mathrm{A_j}(\frac{1-\varepsilon_\mathrm{w}}{\mathrm{A_i}\varepsilon_\mathrm{w}}+\frac{1}{\mathrm{A_i}\mathrm{F_{ij}}}+\frac{1-\varepsilon_\mathrm{p}}{\mathrm{A_j}\varepsilon_\mathrm{p}})}$$

The temperature of the polymer obtained at the end of previous iteration is used as the temperature T_j. Using equations 4.12, 4.13

$$\mathbf{T_{j+1}}\left(-\frac{\mathbf{k}}{\mathbf{\rho c w_j dz^2}}+\left(\frac{\mathbf{k}}{\mathbf{2\rho c w_j{}^2 dz}}\frac{\mathbf{dw}}{\mathbf{dz}}\right)+\frac{\mathbf{1}}{\mathbf{2dz}}\right)+\mathbf{T_j}\left(\frac{\mathbf{2k}}{\mathbf{\rho c w_j dz^2}}+\frac{\mathbf{2h}}{\mathbf{\rho c R_j w_j}}+\frac{\mathbf{2}\boldsymbol{hr_j}}{\mathbf{\rho c R_j w_j}}\right)$$

$$-\ \mathbf{T_{j-1}}\left(\frac{\mathbf{k}}{\mathbf{\rho c w_j dz^2}}+\left(\left(\frac{\mathbf{k}}{\mathbf{2\rho c w_j{}^2 dz}}\frac{\mathbf{dw}}{\mathbf{dz}}\right)+\frac{\mathbf{1}}{\mathbf{2dz}}\right)\right)=\frac{\mathbf{2hTw}}{\mathbf{\rho c R_j w_j}}+\frac{\mathbf{2qw_j}}{\boldsymbol{\rho c}\mathbf{R_j w_j}}$$

At z=0,

$$\frac{T_2-T_{-1}}{2dz}=\left(\frac{w}{2\alpha}+\sqrt{\left(\frac{w}{2\alpha}\right)^2+\frac{2h_a}{kR}}\right)(T(0)-T_a)$$

At z = L,

$$T_{L+dz}+T_{L-d}\ -2T_L=0$$

$$T_{L+dz}=2T_L-T_{L-dz}$$

Step 4

We return to step 2 with the temperature profile obtained in step 3 and calculate an updated velocity profile. This process is repeated until convergence is reached.

Chapter 5 : **Numerical Predictions and Conclusions**

This chapter presents the predictions of the 1-D model. In the first part of this chapter we look at the iterative and grid convergence, in the later part the parametric study of feed speed, peak wall temperature and the draw speed are presented. The results presented here include view factors, heat transfer and the comparison of free surface shape. We also look at the possible reasons for error and end the chapter with conclusions and possible future work.

Convergence criteria

Numerical convergence is monitored by using the norms produced for T at the end of each iteration. Equation 5.1 shows an example calculation of the norm for T, where T_{new} is the temperature profile at the end of the current iteration, and T is temperature profile at the end of the previous iteration.

$$\mathrm{Norm(T)} = \max(\mathrm{abs}(\mathrm{T_{new}} - \mathrm{T})) \tag{5.1}$$

The absolute value of the difference is calculated at each point and the maximum value is taken as the Norm (T). The convergence limit for the temperature norm is 0.1.

Figure 5.1 shows the convergence of free surface shape and **figure 5.2** shows the convergence of temperature profile.

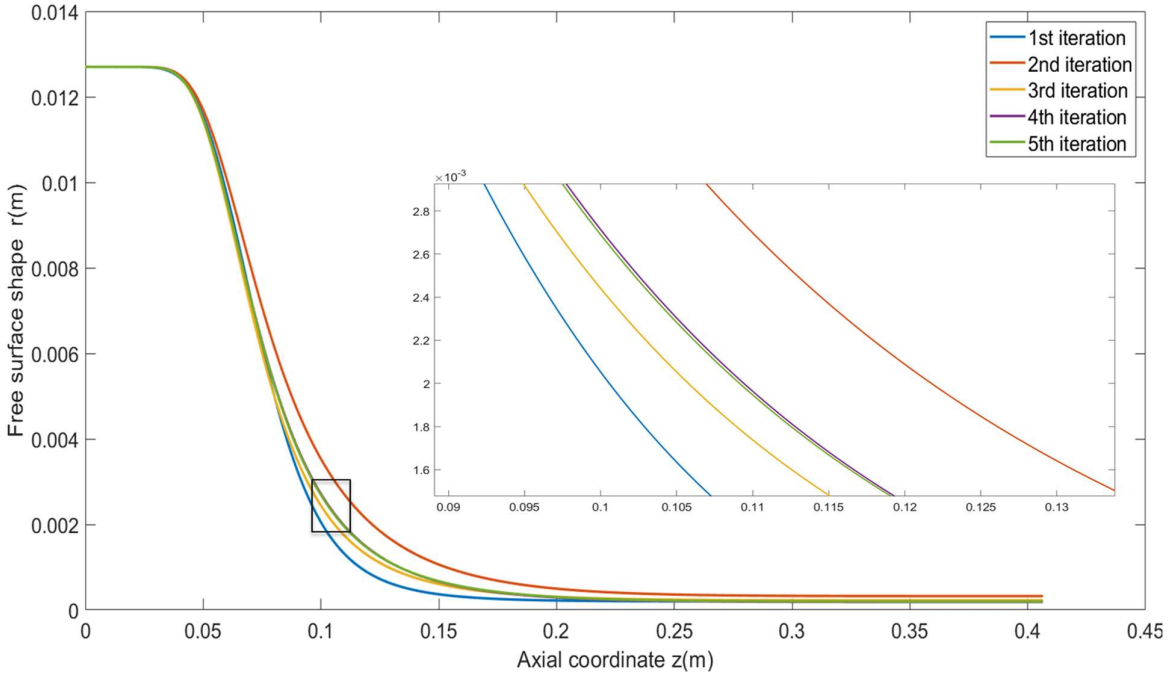

Figure 5.1: Convergence of free surface shape

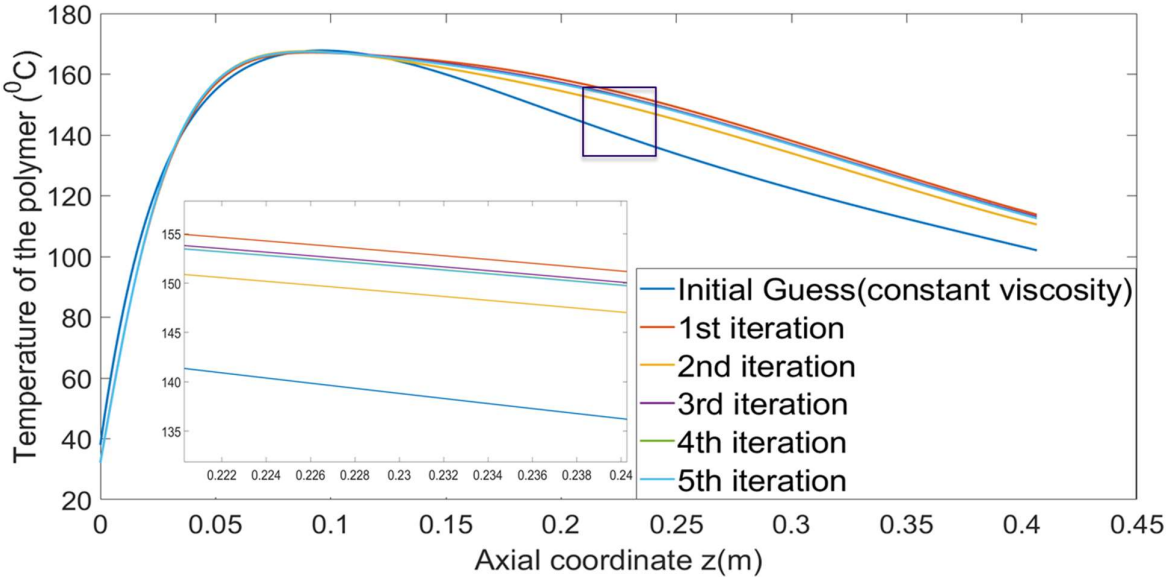

Figure 5.2: Convergence of the temperature profile of the polymer

Parametric study

A parametric study is conducted to determine how independent variables will impact a dependent variable under the given set of assumptions. In a parametric study, the changes in the dependent variable are investigated by perturbing the independent variable. In this section,

the effect of feed speed, peak temperature, and draw speed on the free surface shape are presented.

Feed Speed variation

The effect of feed speed on the free surface shape and polymer temperature is studied by decreasing the feed speed from 45 µm/sec to 25 µm/sec. **Figure 5.3** shows the temperature profile of the polymer, maximum polymer temperature for the case of 25 µm/sec is higher as compared to other higher velocities. **Figure 5.3** also shows that the maximum temperature of the polymer occurs upstream for the case of 25 µm/sec. As a result, the polymer necks down at an earlier axial location this can be observed in **figure 5.4** as the polymer necks down much earlier for the case of 25 µm/sec.

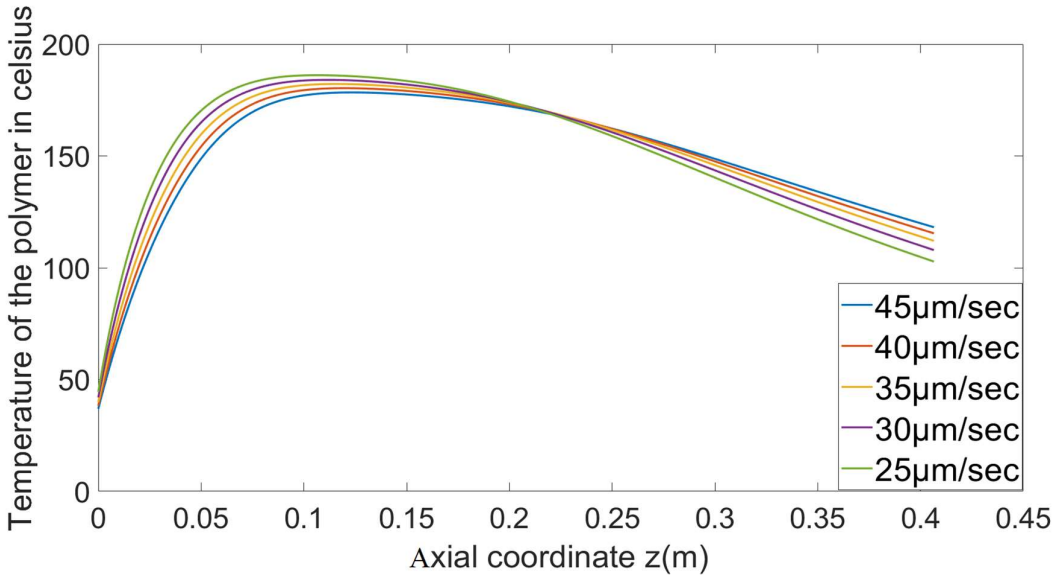

Figure 5.3: Variation of polymer temperature profile with change in the feed speed

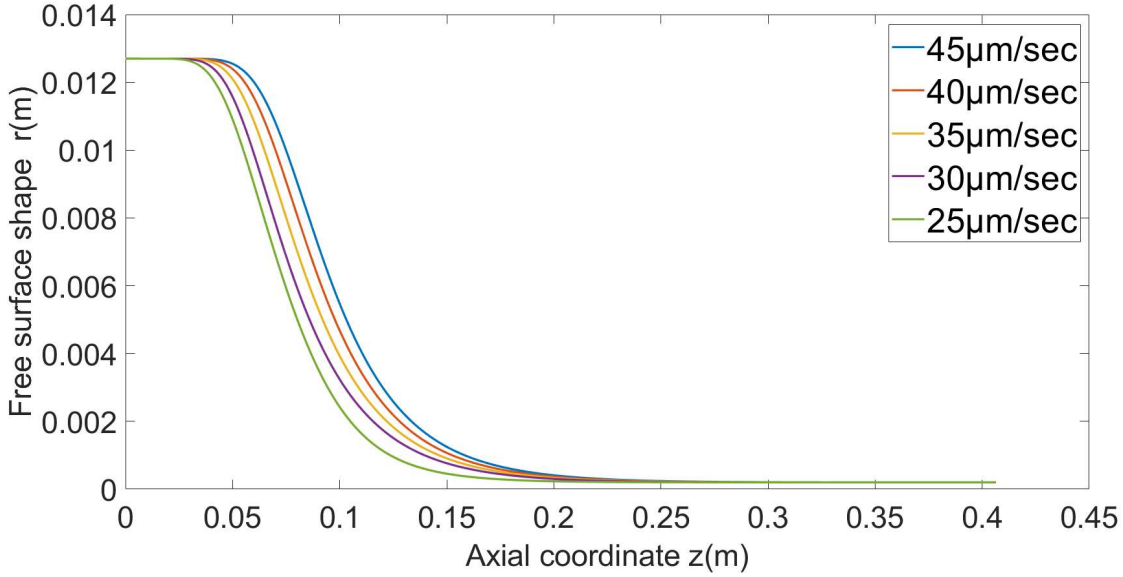

Figure 5.4: Variation of Free surface shape with changes in feed speed

Peak wall temperature

The effect of peak wall temperature on the polymer temperature profile and free surface radius is studied by increasing the maximum wall temperature from 190^0C to 210^0C. The polymer temperature profile for each wall temperature profile can be seen in **figure 5.5**. The increase in the wall temperature increases the heat transfer to the polymer and leads to an earlier neck down region as shown f**igure 5.6.**

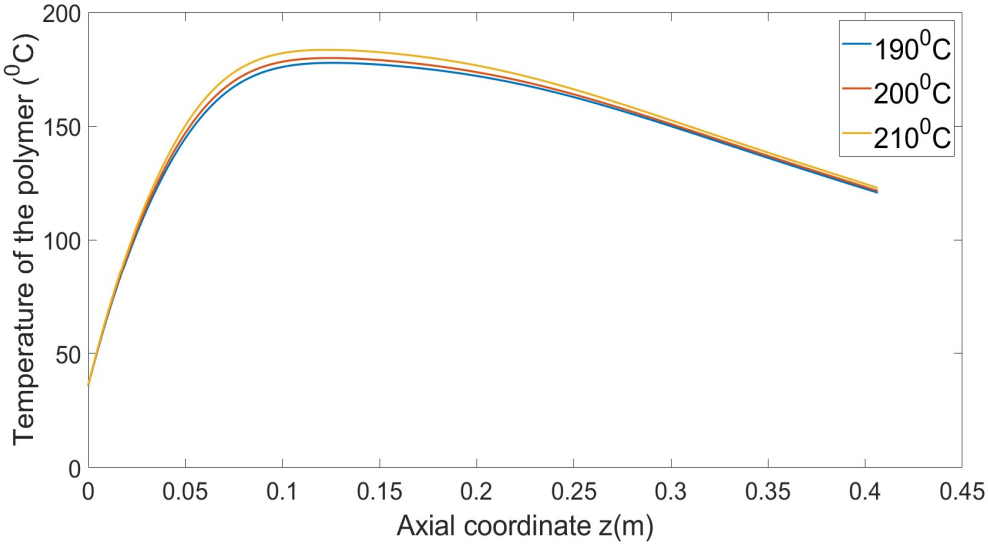

Figure 5.5: Variation of polymer temperature profile with change in the peak furnace temperature

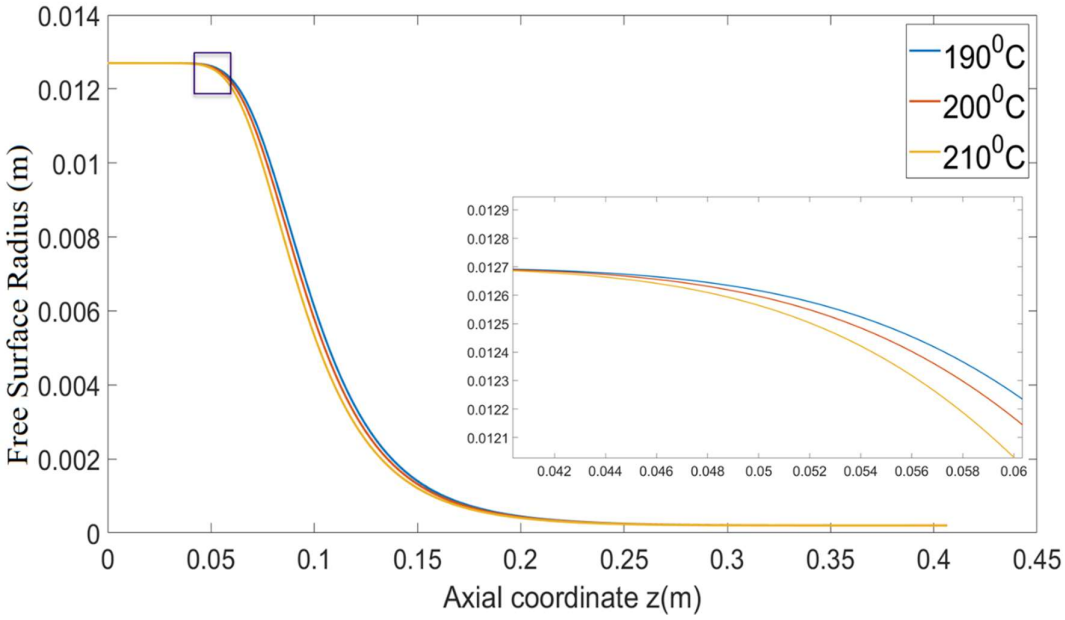

Figure 5.6: Variation of free surface shape with change in the peak wall temperature

Draw speed variation

The effect of draw speed on the polymer temperature and free surface radius is studied by increasing the draw speed from 40cm/sec to 150cm/sec. **Figure 5.7** shows neither that maximum temperature, nor its location is affected by changes in the draw speed. The effect of draw speed can be seen much later during the cooling of the polymer, the increase in the velocity increases the heat loss from the polymer, and thus the exit temperature of the fiber is higher for the case of 40 cm/sec draw speed. **Figure 5.8** shows the free surface shape for each draw speed. The location of neck-down region remained unchanged for each of the different draw speeds, since heat transfer before the neck down region remained unchanged. An increase in the draw speed decreases the exit fiber diameter due to the conservation of mass.

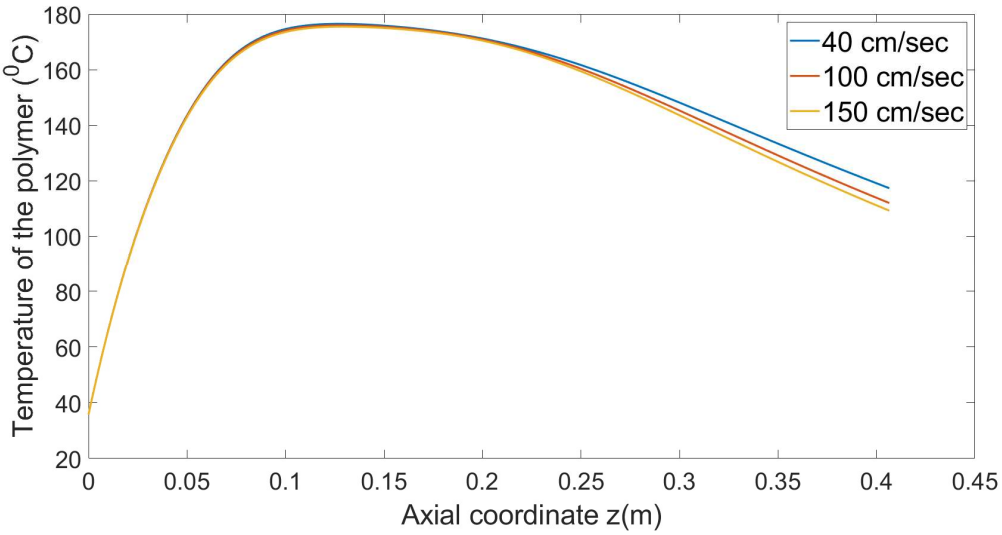

Figure 5.7: Variation of polymer temperature profile with change in the draw speed

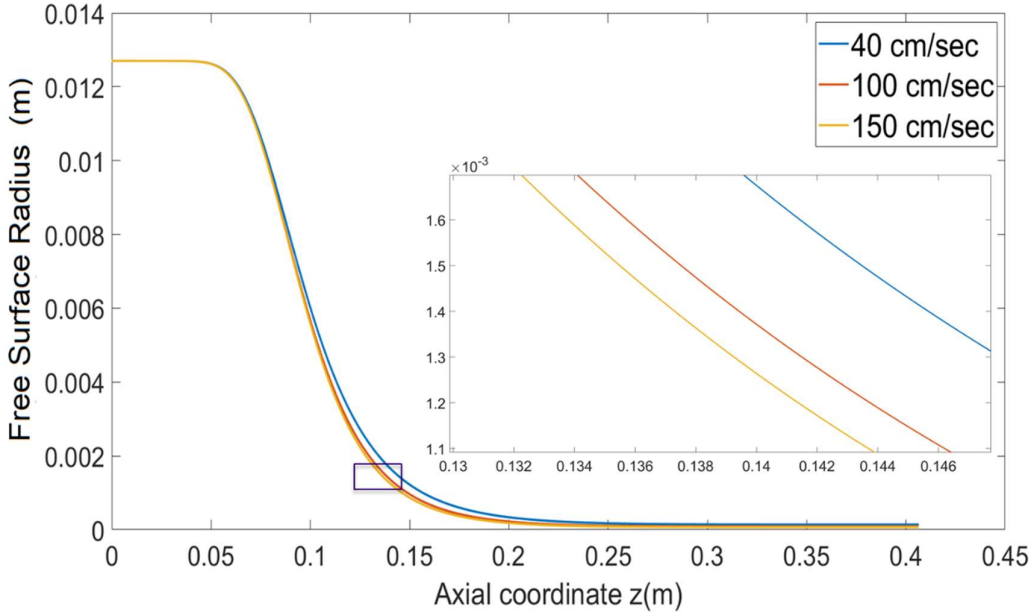

Figure 5.8: Variation of free surface shape with change in the draw speed

Heat transfer results

Figure 5.9 shows the view factors from the furnace element (x-axis) to the 1st polymer element, 100th polymer element, and for 200th polymer element for the case of E1. The maximum view factor occurs when the polymer element and the furnace element are concentric.

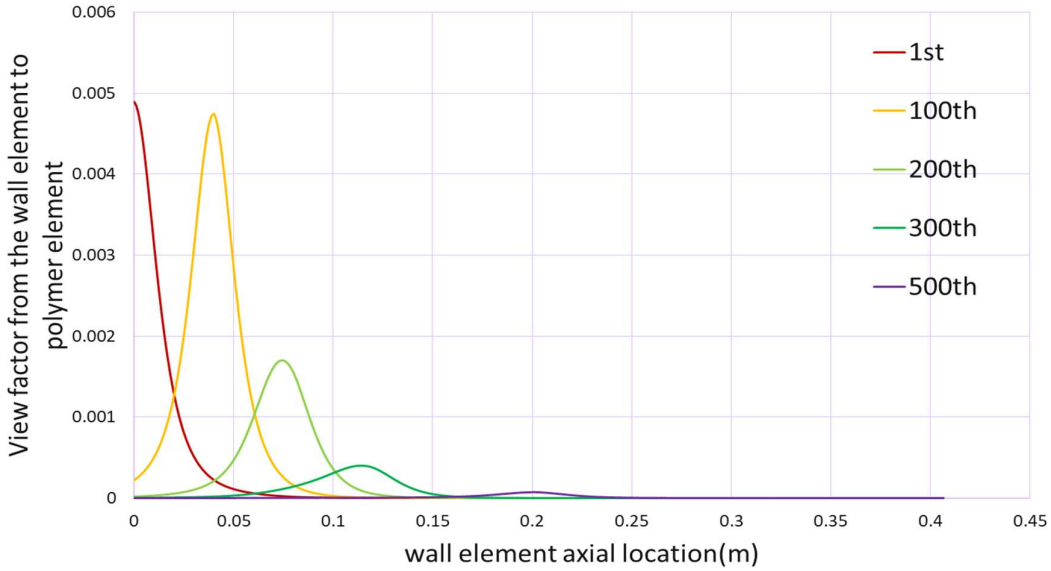

Figure 5.9: View factor from the furnace wall element to the polymer element

Since the radius of the polymer decreases as we go along the furnace, the maximum view factor also decreases as shown in **figure 5.9**. The decrease in the maximum view factor is not linear, there is very little change in the max view factor between 1st polymer element and 100th polymer element, but the max view factor is quickly drops between 100th to 200th and 300th polymer element. This happens because the radius change is very little before the neck-down region, but the radius drops quickly after the neck down region, and so does the maximum view factor. The radiation heat transfer between the polymer element and the furnace elements is shown in **figure 5.10** for the case of E1. The temperature of 300th polymer element is more than the most of the furnace elements, so that is why the net radiation is between the most furnace elements and the 300th polymer element is negative.

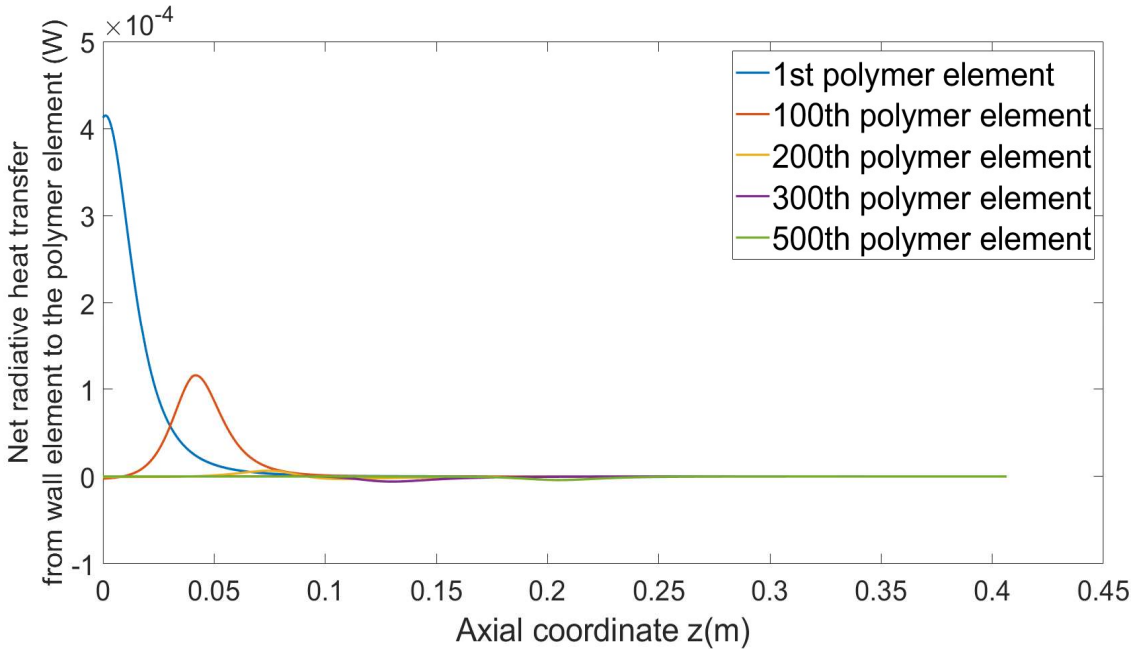

Figure 5.10: The radiation heat transfer between the polymer element and the furnace element at each axial position

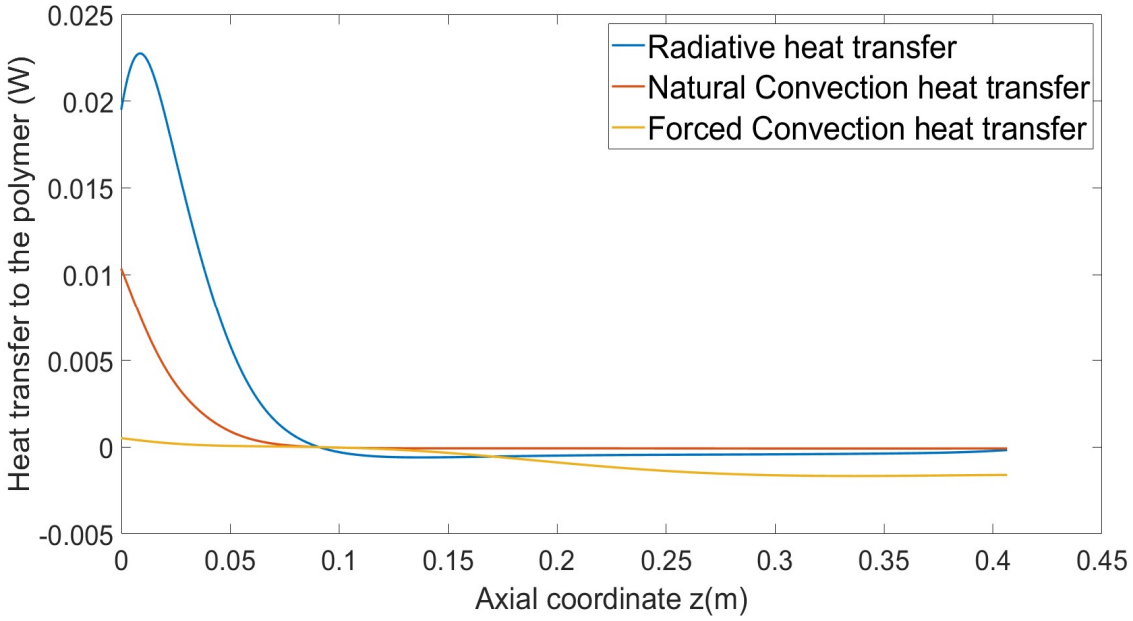

Figure 5.11: The heat transfer due to all three modes along the axial coordinate

The heat transfer to the polymer due the radiation and convection is shown in **figure 5.11** along the axial coordinate. The figure shows preform heating and fiber cooling. The contributions of natural convection heat transfer, radiation heat transfer and forced convection heat transfer are shown in **figure 5.12** for E1**.** The contribution of radiation during the polymer heating is 82% and during the fiber cooling is 26%. The two-dimensional simulations from Reeve et al[16]

predicts that radiation accounts for 70% during the polymer heating and 15% during the polymer cooling.

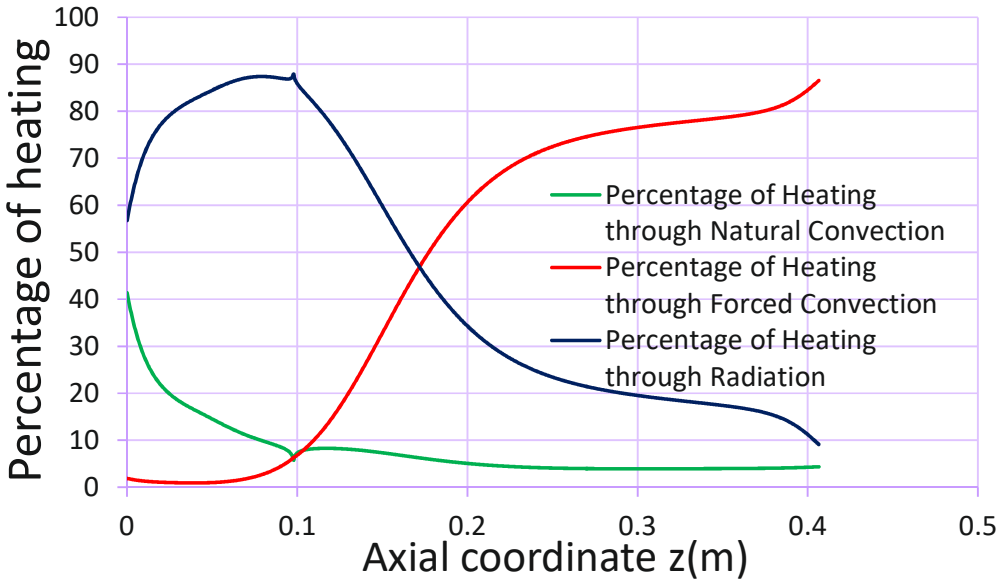

Figure 5.12: Contribution of different modes of heat transfer to the total heating and cooling of the polymer

Peclet number is defined as the ratio of thermal energy convected to a fluid with respect to the thermal energy conducted with in the fluid. **Figure 5.13** shows the axial variation Peclet number. The Peclet number is 3.8 at the start of the drawing and increases up to 350 at the end of the furnace. If the Peclet number is greater than 10, the axial conduction can be neglected from the analysis. From **figure 5.13**, the axial conduction is negligible as the fiber exits the furnace.

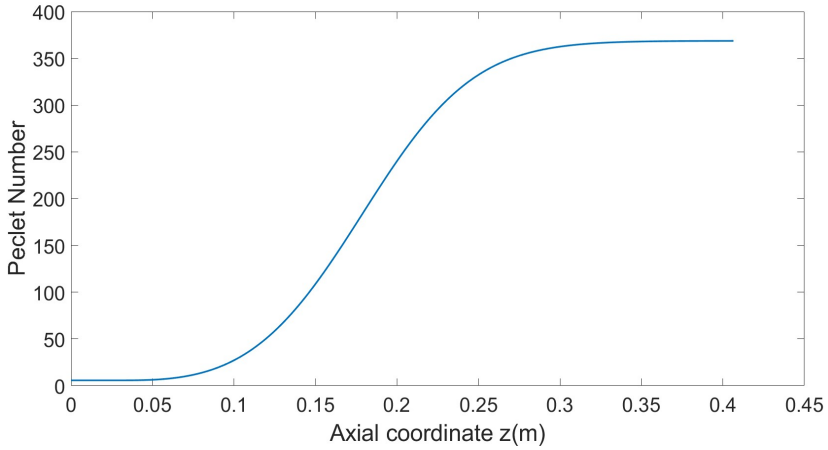

Figure 5.13: Axial variation of Peclet number for E1

Comparison of results from the simplified model to the previous literature

Figure 5.14 shows the comparison of the temperature profile from 1-D model and the centreline temperature (at r=0) and surface temperature from the 2-D simulation of Reeve et al[16] for E1 using correlations from Thomas and Davies while **figure 5.16** is obtained by using correlations from Kehyani et al[33]. The maximum error in the temperature profile w.r.t the centreline temperature profile is 10% in both cases

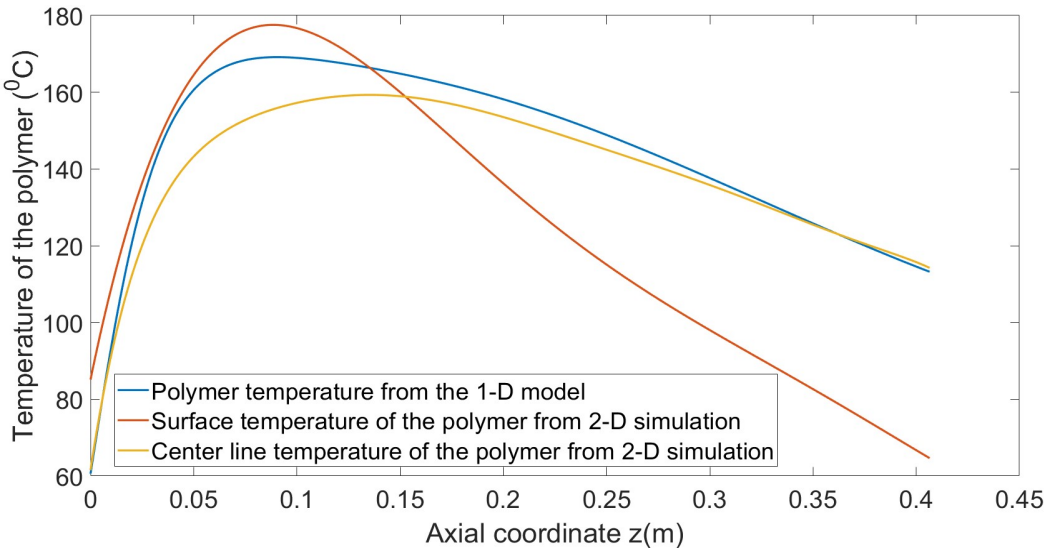

Figure 5.14: Comparison of temperature profile with the surface temperature and centreline temperature of the polymer from 2-D simulation for E1 using correlations from Davies and Thomas[23]

The free surface shape is compared to the experimental and 2-D simulation from Reeve et al[16].

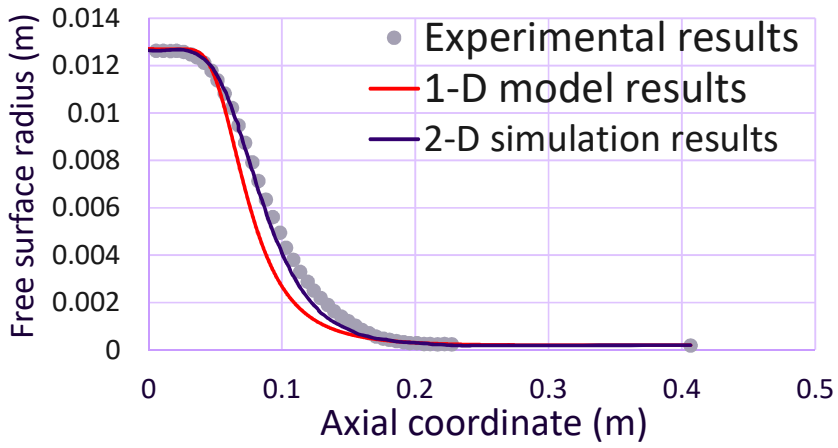

Figure 5.15: Comparison of free surface shape for the case of E1 using correlations from Davies and Thomas[23]

The free surface shape in **figure 5.15** is obtained by using correlations from Thomas and Davies[23], **figure 5.17** is obtained using correlations from Kehyani et al[33]. The maximum error here is 45% w.r.t to the experimental free surface shape in **figure 5.15**, the maximum error is 40%.

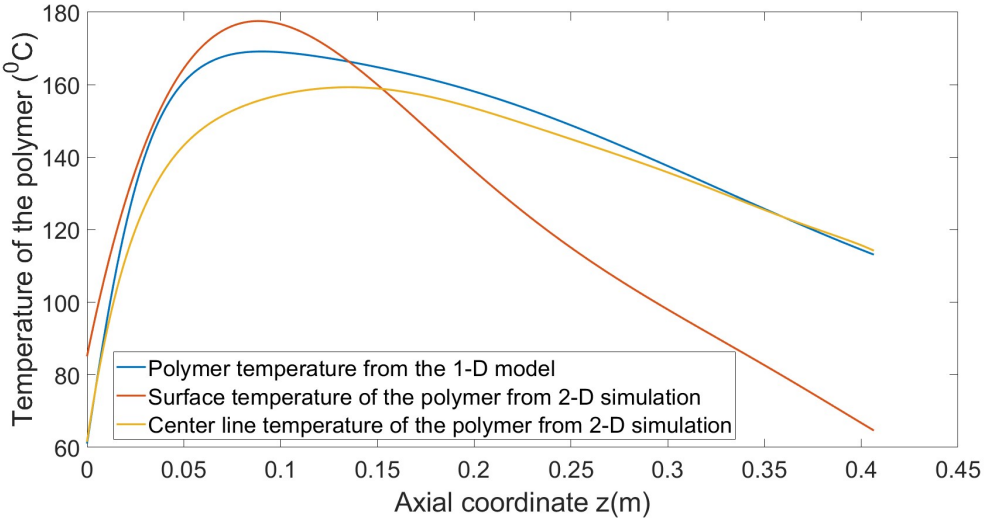

Figure 5.16: Comparison of temperature profile with the surface temperature and centreline temperature of the polymer from 2-D simulation for E1using correlations from Keyhani et al[33]

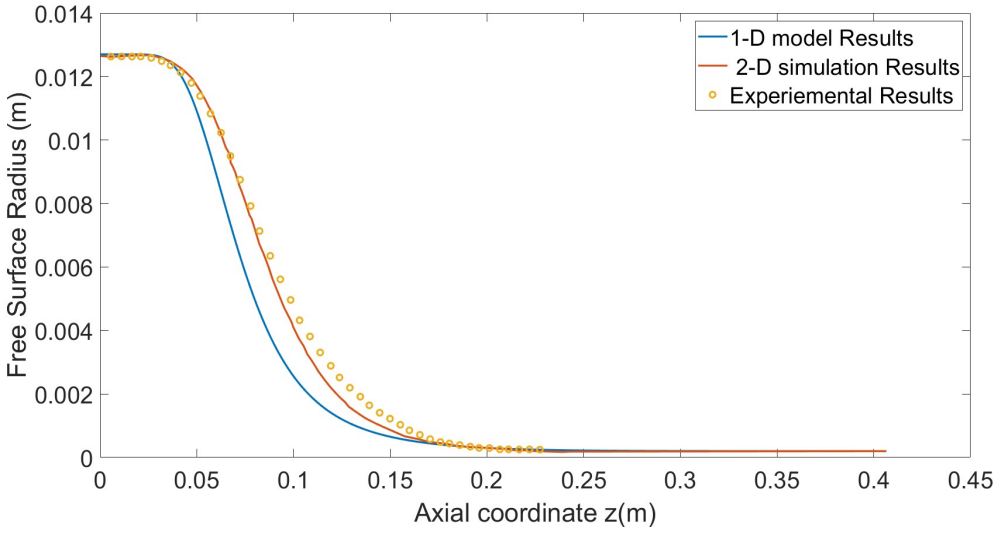

Figure 5.17: Comparison of free surface shape for the case of E1 using correlations from Keyhani et al[33]

Similarly, **figures 5.18 and 5.20** shows the temperature profile for the case E2. **Figure 5.19, 5.21** shows the free surface shape for the corresponding correlations.

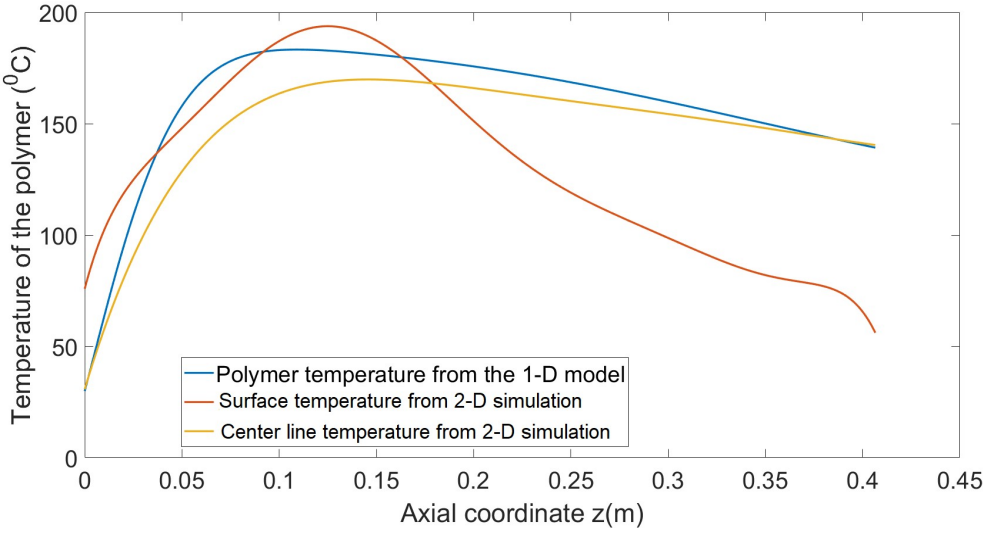

Figure 5.18: Comparison of temperature profile with the surface temperature and centreline temperature of the polymer from 2-D simulation for E2 using correlations from Davies and Thomas[23]

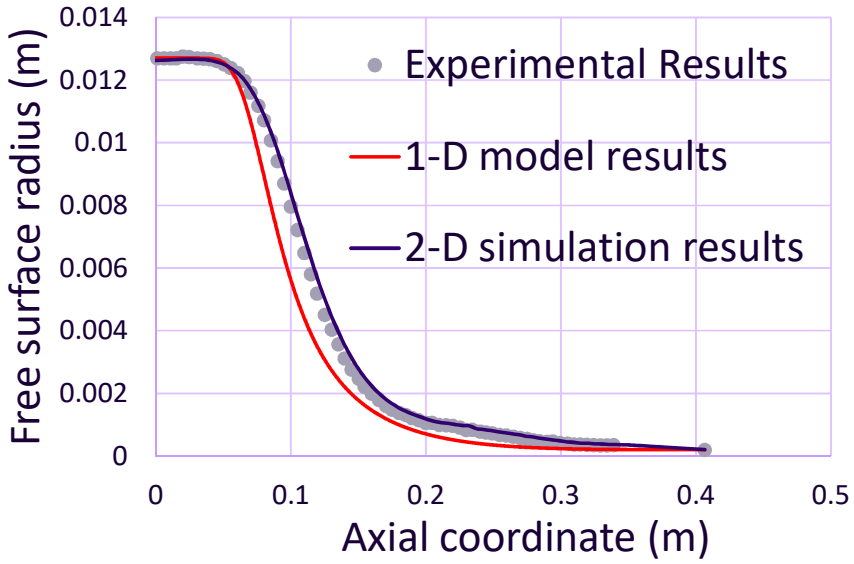

Figure 5.19: Comparison of free surface shape for the case of E2 using correlations from Davies and Thomas[23]

The maximum error in the temperature profile w.r.t the centreline temperature profile is 10% in both cases. The maximum error in the free surface shape is 60% and 55% w.r.t experimental free surface shape for **Figure 5.19, 5.21** respectively.

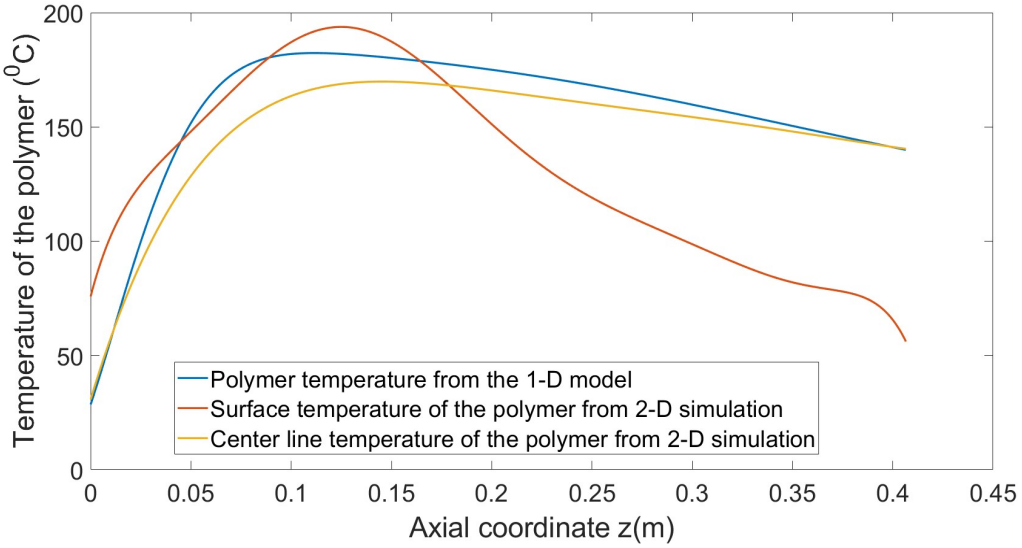

Figure 5.20: Comparison of temperature profile with the surface temperature and centreline temperature of the polymer from 2-D simulation for E2 using correlations from Keyhani et al[33]

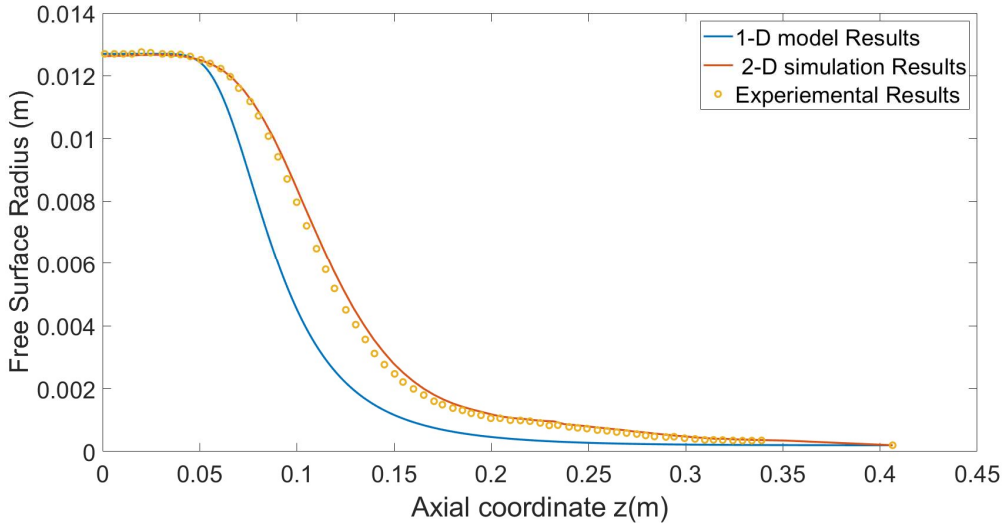

Figure 5.21: Comparison of free surface shape for the case of E2 using correlations from Keyhani et al[33]

Figures 5.22 and **5.23** shows the comparison of free surface shape for E3 case using Thomas and Davies[23], Kehyani et al[33] respectively. The maximum error in each of these cases are 43% and 36%.

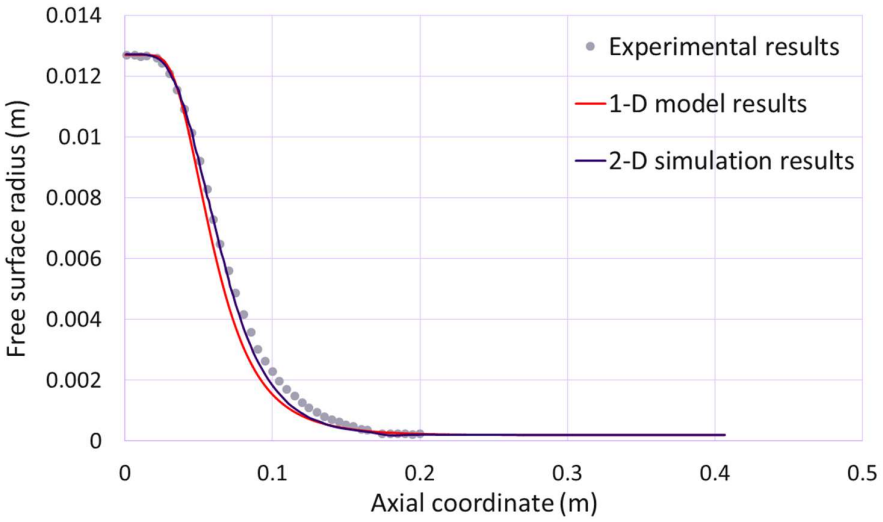

Figure 5.22: Comparison of free surface shape for the case of E3 using correlations from Thomas and Davies[23]

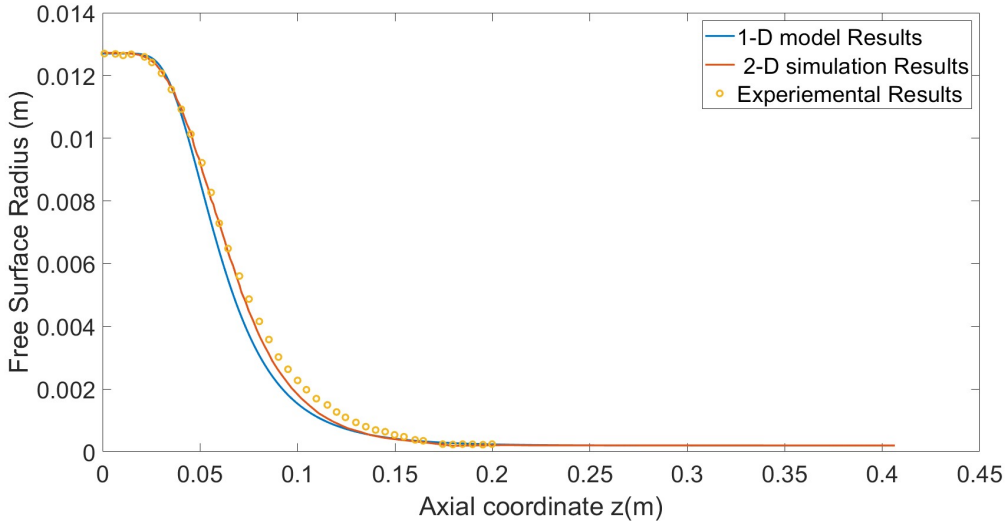

Figure 5.23: Comparison of free surface shape for the case of E3 using correlations from Keyhani et al

Figures 5.24 and **5.25** shows the comparison of free surface shape for E4 case using Thomas and Davies[23], Kehyani et al[33] respectively. The maximum error in each of these cases are 54% and 50%.

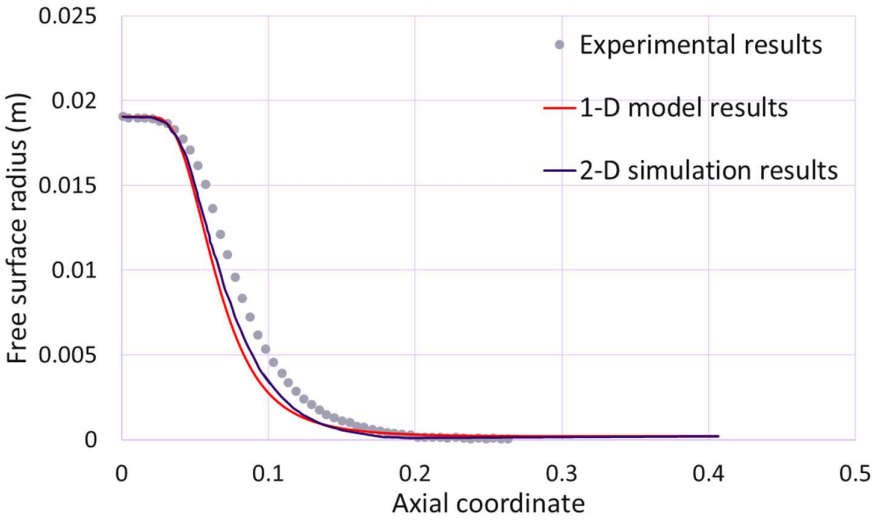

Figure 5.24: Comparison of free surface shape for the case of E4 using correlations from Thomas and Davies[23]

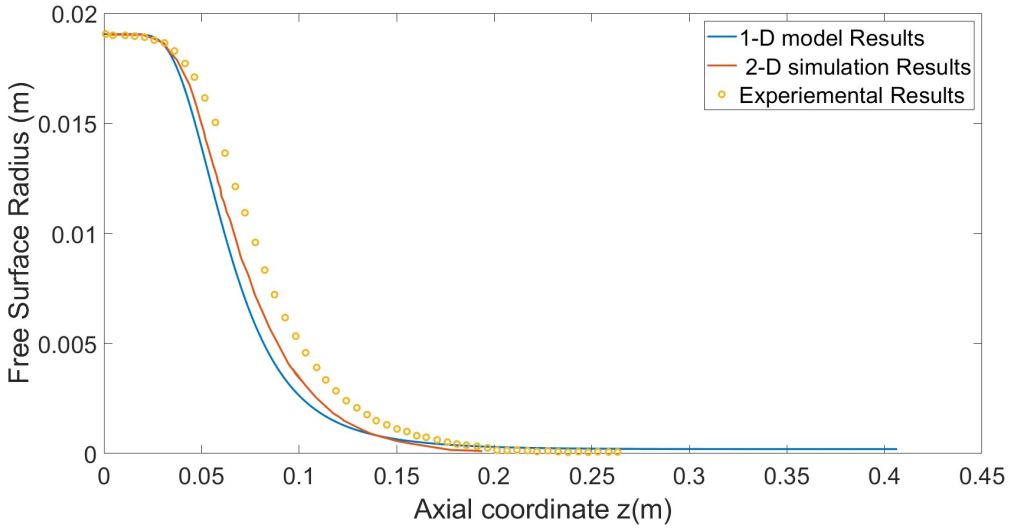

Figure 5.25: Comparison of free surface shape for the case of E4 using correlations from Keyhani et al

The temperature profile obtained from the numerical model gives a good agreement with the 2-D simulations, while the free surface shape shows a considerable error.

Sources for the error

Error due to the assumption of 1-D model or lumped capacity model.

The accuracy of the lumped capacity model is determined by Biot number (equation 5.2). Biot number is defined as the ratio of the internal conductive resistance to the external resistance.

This ratio determines the variation of temperature inside a body while the body heats due to the heat transfer to the surface of the body.

$$Bi = \frac{hR}{2k} \tag{5.2}$$

Here h is the heat transfer coefficient, R is the radius of the cylinder and k is the thermal conductivity of the polymer.

Figure 5.26 shows the axial variation of Biot number for the case of E1. Traditionally, when calculating the Biot number only the convective heat transfer coefficient is used, but in the simplified model, radiation heat transfer also heats the polymer through surface heating. If the Biot number is less that 0.1 then the error in the lumped capacity model will be less than 5%. The Biot number plot indicates that the 1-D model is inadequate in predicting to predict the free surface shape.

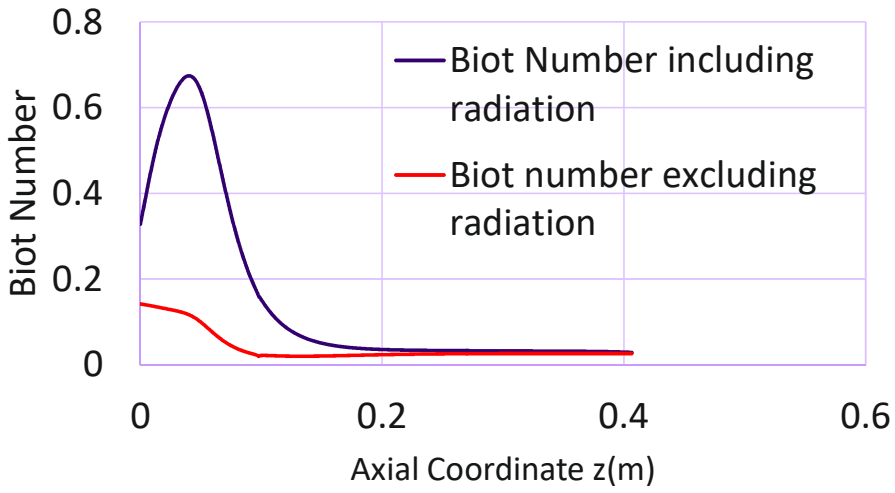

Figure 5.26: Axial variation of Biot Number for E1

Error due to the empirical relation for natural convection heat transfer coefficient

The empirical relation given for natural convection heat transfer coefficient given by equation 3.10 is obtained for natural convection of fluid between two concentric isothermal cylinders. In the simplified model, the radius of the polymer is not constant. The temperature of the

furnace and temperature of the polymer are not constant either. By using a different heat transfer coefficients we can get better comparison with the experimental free surface radius.

Conclusions

The parametric study indicates that numerical model can robustly predict the effect of each of the operating conditions. The radiation heat transfer and the view factor estimated by the numerical model are in line with the physical intuition. While the model does give us a considerable error in the prediction of free surface shape, this results are not discouraging. By using the temperature profile and the free surface shape as initial guess for 3-D simulations, the convergence times can be significantly reduced.

Future work

The polymer is most susceptible to the gas phase oscillations during the latter part of the neck down region due to the low polymer viscosity and thermal mass (from z = 0.1m to 0.2m in the **figures 5.15, 5.19, 5.22, 5.24**). The Biot number is less than 0.1 for the corresponding axial location as shown in **figure 5.26**. So a transient lumped capacity model with frequency of the gas phase oscillations can be used to estimate the exit diameter variations.

Chapter 6 : **Summary**

A quasi one dimensional method was used to model the polymer preform as it necks down to optical fiber in a heated furnace. Conservation equations were derived for a control volume which is lumped across the radial direction and differential along the axial coordinate. Constant feed speed at the inlet and draw speed at the exit are used as the momentum boundary conditions. For the thermal boundary conditions, the preform is modeled as moving infinite fin at the inlet and zero thermal diffusion at the exit. The highly coupled non-linear conservation equations were solved using iterative method with RK45 and finite difference. The iterative process is continued until the convergence criteria is reached. The error in the numerical method is of second order.

Empirical relation from Thomas and Davies[23] and Keyhani et al[33] were used for the natural convection heat transfer coefficient.. Empirical relation from Kase and Matsuo[11] was used for the forced convection heat transfer coefficient, which depends on the Reynolds number. The view factor from the each furnace element to the polymer element was calculated using Reid and Tennet[29] for coaxial elements and Leuenberger and Person[30] for the concentric elements. The radiation heat transfer between the each furnace element and the polymer elements are calculated using enclosure analysis.

A parametric study was conducted to study to effect of feed speed, draw speed and peak temperature on the free surface shape of the polymer and the temperature of the polymer. The numerical method predicts that during the heating of the polymer, the radiation heating accounts for 80% and during the cooling of the polymer the radiation accounts for 26% of the cooling of the polymer.

REFERENCES

1. GLICKSMAN, L. R. (1968). THE DYNAMICS OF A HEATED FREE JET OF VARIABLE VISCOSITY LIQUID AT LOW REYNOLDS NUMBERS. JOURNAL OF BASIC ENGINEERING, 90(3), 343-354.
2. PAEK, U. C., & RUNK, R. B. (1978). PHYSICAL BEHAVIOR OF THE NECK-DOWN REGION DURING FURNACE DRAWING OF SILICA FIBERS. JOURNAL OF APPLIED PHYSICS, 49(8), 4417-4422.
3. VASILJEV, V. N., DULNEV, G. N., & NAUMCHIC, V. D. (1989). FLOW OF HIGHLY VISCOUS LIQUID WITH A FREE SURFACE. GLASS TECHNOLOGY, 30(2), 83-90.
4. LEE, S. H. K., & JALURIA, Y. (1995). THE EFFECTS OF GEOMETRY AND TEMPERATURE VARIATIONS ON THE RADIATIVE TRANSPORT DURING OPTICAL FIBER DRAWING. JOURNAL OF MATERIALS PROCESSING & MANUFACTURING SCIENCE, 3(4), 317-331.
5. LEE, S. K., & JALURIA, Y. (1996). EFFECTS OF VARIABLE PROPERTIES AND VISCOUS DISSIPATION DURING OPTICAL FIBER DRAWING. JOURNAL OF HEAT TRANSFER, 118(2), 350-358.
6. LEE, S. H. K., & JALURIA, Y. (1997). SIMULATION OF THE TRANSPORT PROCESSES IN THE NECK-DOWN REGION OF A FURNACE DRAWN OPTICAL FIBER. INTERNATIONAL JOURNAL OF HEAT AND MASS TRANSFER, 40(4), 843-856.
7. CHOUDHURY, S. R., & JALURIA, Y. (1998). PRACTICAL ASPECTS IN THE DRAWING OF AN OPTICAL FIBER. JOURNAL OF MATERIALS RESEARCH, 13(2), 483-493.
8. CHOUDHURY, S. R., & JALURIA, Y. (1998). THERMAL TRANSPORT DUE TO MATERIAL AND GAS FLOW IN A FURNACE FOR DRAWING AN OPTICAL FIBER. JOURNAL OF MATERIALS RESEARCH, 13(2), 494-503.
9. PAPAMICHAEL, H., PELLON, C., & MIAOULIS, I. N. (1997). AIR FLOW PATTERNS IN THE OPTICAL FIBRE DRAWING FURNACE. GLASS TECHNOLOGY, 38(1), 22-29.
10. S. KASE AND T.MATSUO, STUDIES ON MELT SPINNING. I. FUNDAMENTAL EQUATIONS ON THE DYNAMICS OF MELT SPINNING, J. POLYMER SCIENCE: PART A, 3 (1965), 2541-2554.
11. S. KASE AND T.MATSUO, STUDIES ON MELT SPINNING. II. STEADY-STATE AND TRANSIENT SOLUTIONS OF FUNDAMENTAL EQUATIONS COMPARED WITH EXPERIMENTAL RESULTS, JOURNAL OF APPLIED POLYMER SCIENCE, 11 (1967), 251-287.
12. KASE, S. (1974). STUDIES ON MELT SPINNING. III. VELOCITY FIELD WITHIN THE THREAD. NAKAMURA, K., KATAYAMA, K., & AMANO, T. (1973). SOME ASPECTS OF NON-ISOTHERMAL CRYSTALLIZATION OF POLYMERS. II. CONSIDERATION OF THE ISOKINETIC CONDITION. JOURNAL OF APPLIED POLYMER SCIENCE, 17(4), 1031-1041.
13. CHUNG, B. T., & IYER, V. (1992). HEAT TRANSFER FROM MOVING FIBERS IN MELT SPINNING PROCESS. JOURNAL OF APPLIED POLYMER SCIENCE, 44(4), 663-670.
14. REEVE, H. M., & MESCHER, A. M. (1999). A STUDY ON TRANSIENT HEATING OF POLYMER FIBER PREFORMS. JOURNAL OF MATERIALS PROCESSING AND MANUFACTURING SCIENCE, 8, 94-105.
15. REEVE, H. M., MESCHER, A. M., & EMERY, A. F. (2004). INVESTIGATION OF STEADY-STATE DRAWING FORCE AND HEAT TRANSFER IN POLYMER OPTICAL FIBER MANUFACTURING. JOURNAL OF HEAT TRANSFER, 126(2), 236-243.
16. REEVE, H. M. (2004). EFFECT OF NATURAL CONVECTION HEAT TRANSFER DURING POLYMER OPTICAL FIBER DRAWING.
17. TETSU, F., & HARUO, U. (1970). LAMINAR NATURAL-CONVECTIVE HEAT TRANSFER FROM THE OUTER SURFACE OF A VERTICAL CYLINDER. INTERNATIONAL JOURNAL OF HEAT AND MASS TRANSFER, 13(3), 607-615.

18. NAGENDRA, H. R., TIRUNARAYANAN, M. A., & RAMACHANDRAN, A. (1970). LAMINAR FREE CONVECTION FROM VERTICAL CYLINDERS WITH UNIFORM HEAT FLUX. JOURNAL OF HEAT TRANSFER, 92(1), 191-194.
19. NAGENDRA, H. R., TIRUNARAYANAN, M. A., & RAMACHANDRAN, JOURNAL OF THE CHEMICAL ENGINEERING SOCIETY, VOL. 24, 1909, PP.1491.
20. KIMURA, F., TACHIBANA, T., KITAMURA, K., AND HOSOKAWA, T, FLUID FLOW AND HEAT TRANSFER OF NATURAL CONVECTION AROUND HEATED VERTICAL CYLINDERS, JSME INT. JOURNAL, SERIES B, VOL. 47, NO. 2, PP.156–161, 2004
21. CEBECI, T. (1974). LAMINAR-FREE-CONVECTIVE-HEAT TRANSFER FROM THE OUTER SURFACE OF A VERTICAL SLENDER CIRCULAR CYLINDER. IN INTERNATIONAL HEAT TRANSFER CONFERENCE DIGITAL LIBRARY. BEGEL HOUSE INC.
22. POPIEL, C. O. (2008). FREE CONVECTION HEAT TRANSFER FROM VERTICAL SLENDER CYLINDERS: A REVIEW. HEAT TRANSFER ENGINEERING, 29(6), 521-536.
23. THOMAS, R. W., & DE VAHL DAVIS, G. (1970). NATURAL CONVECTION IN ANNULAR AND RECTANGULAR CAVITIES A NUMERICAL STUDY. IN INTERNATIONAL HEAT TRANSFER CONFERENCE DIGITAL LIBRARY. BEGEL HOUSE INC.
24. ANDREWS, E. H. (1959). COOLING OF A SPINNING THREAD-LINE. BRITISH JOURNAL OF APPLIED PHYSICS, 10(1), 39.
25. RA SEBAN. (1951). SKIN-FRICTION AND HEAT-TRANSFER CHARACTERISTICS OF A LAMINAR BOUNDARY LAYER ON A CYLINDER IN AXIAL INCOMPRESSIBLE FLOW. JOURNAL OF THE AERONAUTICAL SCIENCES, 18(10), 671-675.
26. RICHELLE, E., TASSE, R., & RIETHMULLER, M. L. (1995). MOMENTUM AND THERMAL BOUNDARY LAYER ALONG A SLENDER CYLINDER IN AXIAL FLOW. INTERNATIONAL JOURNAL OF HEAT AND FLUID FLOW, 16(2), 99-105.
27. EIDINGER, A. T. C. (2006). MODELING THE EFFECTS OF SURFACE TENSION IN POLYMER CAPILLARY FIBER (DOCTORAL DISSERTATION, UNIVERSITY OF WASHINGTON).
28. "TYPES OF SPINNING (MAN-MADE FIBERS)." TEXTILE ENGINEER @ BLOGSPOT, TEXTILEENGINEERR.BLOGSPOT.COM/2010/10/TYPES-OF-SPINNING-MAN-MADE-FIBERS.HTML.
29. REID, R. L., & TENNANT, J. S. (1973). ANNULAR RING VIEW FACTORS. AIAA JOURNAL, 11(10), 1446-1448.
30. LEUENBERGER, H., & PERSON, R. A. (1954). COMPILATION OF RADIATION SHAPE FACTORS FOR CYLINDRICAL ASSEMBLIES (NO. PAPER-56-A-144).
31. TROUTON, F. T. (1906). ON THE COEFFICIENT OF VISCOUS TRACTION AND ITS RELATION TO THAT OF VISCOSITY. PROCEEDINGS OF THE ROYAL SOCIETY OF LONDON. SERIES A, CONTAINING PAPERS OF A MATHEMATICAL AND PHYSICAL CHARACTER, 77(519), 426-440.
32. KHAN, J. A., & KUMAR, R. (1989). NATURAL CONVECTION IN VERTICAL ANNULI: A NUMERICAL STUDY FOR CONSTANT HEAT FLUX ON THE INNER WALL.
33. KEYHANI, M., KULACKI, F. A., & CHRISTENSEN, R. N. (1983). FREE CONVECTION IN A VERTICAL ANNULUS WITH CONSTANT HEAT FLUX ON THE INNER WALL. *JOURNAL OF HEAT TRANSFER*, *105*(3), 454-459.
34. KUMAR, R., & KALAM, M. A. (1991). LAMINAR THERMAL CONVECTION BETWEEN VERTICAL COAXIAL ISOTHERMAL CYLINDERS. *INTERNATIONAL JOURNAL OF HEAT AND MASS TRANSFER*, *34*(2), 513-524.

Appendix: Numerical Code

Constant Viscosity

```
clear all
clc
h =0.4065;
rho = 1195;
c = 1475;
dz = h/1000;
z = 0:dz:h;
dt = (dz*dz/3);
count = 0;
g = 9.807;
l = length(z);
w = zeros(size(z));
r0 = 0.0127;
u = 2.3*(10^9)/1195;
k1 = 11.835e+7;
w(1) = 50*(10^-6)*0.25;
e1 = 0.96;
r2 = 32*(10^-3);
e2 = 0.75;
sig = (5.67*(10^-8));
ua = 1.48*(10^-5);

for i = 1:l-1
   X = 1./w(1:i);
   R = z(1:i);
   I1 = g*trapz(R,X);
   w(i+1) = w(i)+(dz*(w(i)/(3*u))*(w(i)+k1-I1));
end

r = (w(1)*(r0^2)./w).^(0.5);
temp =63*ones(1,l);
omega = ones(1,l);


Tw = (-630.03*((z/h).^4)) + (1771.4*((z/h).^3)) - (1628.4*((z/h).^2)) +
(389.34*((z/h).^1)) + 145.25; %E1%
hh = hE2;
hc = zeros(size(z));
hr = zeros(size(z));
hn = zeros(size(z));
hx = zeros(size(z));
```

```
Re = 2*w.*r/(1.48*(10^-5));
Nuf = 1*0.42*(Re.^0.334);
hc = ((Nuf*0.03251)./(2*r));


   for ii =1:l-1
      Gf2(ii) = abs(1*g*(Tw(ii)-temp(ii))*((r2-r(1))^3)/((Tw(ii)+273.16)*1*(ua^2)));
       Nun(ii)= 0.775857478680783*(Gf2(ii)^0.101);
       hr(ii) =
sig*(((Tw(ii)+273).^2)+((temp(ii)+273).^2)).*(((Tw(ii)+273))+((temp(ii)+273))).*e_e
(ii);
        hn(ii) = ((Nun(ii)*0.03251)./(1*(r2-r(ii))));
        hx(ii)  = hc(ii)+hr(ii)+hn(ii);
        hh(ii)   = hx(ii);

      temp(ii+1) =temp(ii)+(dz*2*hh(ii)*(Tw(ii)-temp(ii))/(rho*c*r(ii)*w(ii)));
   end
```

Variable Viscosity

```
clc
vm = @(x)((1.506*(10^5)/1195)*(exp(2935*((1./x)-(1/170)))));
km = @(x)((( 0.0698*x) + 24.503)*(10^-3));
h  = 0.4065;
dz = h/1000;
g = 9.8;
u = (2.3*(10^9))/1195;
ua = 1.48*(10^-5);
w0 = 50*(10^-6)*0.25;
e1 = 0.96;
r2 = 32*(10^-3);
e2 = 0.75;
sig = (5.67*(10^-8));
z = 0:dz:h;
Tw = (-630.03*((z/h).^4)) + (1771.4*((z/h).^3)) - (1628.4*((z/h).^2)) +
(389.34*((z/h).^1)) + 145.25; %E1%
r0 = 0.0127;
Gf2 = abs(1*g*(Tw-temp)*((r2-r0)^3)./((Tw+273.16)*1*(ua^2)));
Nun= 0.775857478680783*(Gf2.^0.101);
hn = ((Nun*0.03251)./(r2-r));
e_e = e1./(1+((e1*r/(e1*r2))*(1-e2)));
hr = sig*(((Tw+273).^2)+((temp+273).^2)).*(((Tw+273))+((temp+273))).*e_e;

l = length(z);
y = zeros(2,l);
y(1,1) = w0;
```

```
% w1 =  0.0000001185; %%1st iteration
% w1 =  0.0000001216 ;%%2st iteration
% w1 =  0.00000014835; %%3st iteration
w1 =  0.0000001495; %%4th iteration


hh = hE2;
rho = 1195;
c = 1465;
jjj = 0;
r = zeros(size(z));
Re = zeros(size(z));


y(2,1) = w1;
for ii = 1:l-1
   if temp(ii)<=109

      k1 = dz* velocity(y(:,ii),u,g);
      k11 = y(:,ii)+((k1)/2);
      k2 = dz* velocity(k11,u,g);
      k22 = y(:,ii)+((k2)/2);
      k3 = dz* velocity(k22,u,g);
      k33 = y(:,ii)+((k3)/2);
      k4 = dz* velocity(k33,u,g);
      y(:,ii+1) = y(:,ii) + ((k1+(2*k2)+(2*k3)+k4)/6);
   end
   if temp(ii)>109
      k1 = dz* coupled(y(:,ii),vm,g,temp,ii,dz);
      k11 = y(:,ii)+((k1)/2);
      k2 = dz* coupled(k11,vm,g,temp,ii,dz);
      k22 = y(:,ii)+((k2)/2);
      k3 = dz* coupled(k22,vm,g,temp,ii,dz);
      k33 = y(:,ii)+((k3)/2);
      k4 = dz* coupled(k33,vm,g,temp,ii,dz);
      y(:,ii+1) = y(:,ii)+((k1+(2*k2)+(2*k3)+k4)/6);

   end
end
r = r0*((y(1,1)./y(1,:)).^0.5);

w = y(1,:);
dw = y(2,:);
rr = r;
 Re = 2*w.*r/(1.48*(10^-5));
```

```
Nuf = 1*0.42*(Re.^0.334);
hc = ((Nuf*0.03251)./(2*r));

plot(z,w)


vf = zeros(l,l);
hr1 = zeros(l,l);
hr2 = zeros(l,l);
qr3 = zeros(size(z));
hr4 = zeros(size(z));

for kk = 1:l
for kkk = 1:l


d0 = abs(z(kk)-z(kkk));

vf(kkk,kk) = viewfactor(r2,d0,dz,rr(kkk));
hr1(kkk,kk) = radiation(e2,r2,e1,rr(kkk),sig,Tw(kk),temp(kkk),vf(kkk,kk))*(Tw(kk));
hr2(kkk,kk) = radiation(e2,r2,e1,rr(kkk),sig,Tw(kk),temp(kkk),vf(kkk,kk));
if kkk ==kk
vf(kkk,kk) = adjacent(r(kkk),r2,dz);
hr1(kkk,kk) = radiation(e2,r2,e1,rr(kkk),sig,Tw(kk),temp(kkk),vf(kkk,kk))*(Tw(kk));
hr2(kkk,kk) = radiation(e2,r2,e1,rr(kkk),sig,Tw(kk),temp(kkk),vf(kkk,kk));

end

end
qr3(kk) = sum(hr1(:,kk));
hr4(kk) = sum(hr2(:,kk));


end

hh = hc+hn+hr4;
hh1 = hc+hn;
BT  =  zeros(size(z));
BT = transpose(BT);
AT = zeros(l,l);
ccc1  = 0.5*rho*c*w(1)*dz/0.193;
ccc2 = 0.5*dw(1)*dz/w(1);
ccc3 = 2*hh(1)*dz*dz/(0.193*r(1));
ccc4 = 2*hh1(1)*dz*dz/(0.193*r(1));
AT(1,1) =2+ccc3+(163.3403*2*dz*(ccc1+ccc2+1));
AT(1,2) =-2;
```

```
BT(1) =
ccc4*Tw(1)+(23*163.3403*2*dz*(ccc1+ccc2+1))+((2*qr3(1)*dz*dz)/(0.193*r(1)));


for jj = 2:l-1

    ccc1  = 0.5*rho*c*w(jj)*dz/0.193;
    ccc2 = 0.5*dw(jj)*dz/w(jj);

    ccc3 = 2*hh(jj)*dz*dz/(0.193*r(jj));
    ccc4 = 2*hh1(jj)*dz*dz/(0.193*r(jj));
    AT(jj,jj) = 2+ccc3;
    AT(jj,jj+1) = ccc1+ccc2-1;
    AT(jj,jj-1) = -1*(ccc1+ccc2+1);
    BT(jj) = ccc4*Tw(jj)+((2*qr3(jj)*dz*dz)/(0.193*r(jj)));
end
ccc1  = 0.5*rho*c*w(end)*dz/0.193;
ccc2 = 0.5*dw(end)*dz/w(end);
ccc3 = 2*hh(end)*dz*dz/(0.193*r(end));
ccc4 = 2*hh1(end)*dz*dz/(0.193*r(end));
AT(end,end-1) = (-ccc1-ccc2)*2;
AT (end,end) = (2*ccc1)+(2*ccc2)+ccc3;
BT(end) = ccc4*Tw(end)+((2*qr3(end)*dz*dz)/(0.193*r(end)));
Tnew = transpose(AT\BT);

 plot(z,w)


function dy =  velocity(y,u,g)
A = [y(2);(((y(2)*y(1))/(3*u)))+((y(2)^2)/y(1))] + [0;(-g/(3*u))];
dy = A;
end
function dk =  coupled(y,vm,g,temp,ii,dz)
B =
[y(2);(((y(2)*y(1))/(3*vm(temp(ii)))))+((y(2)^2)/y(1))+((y(2)*2935/((temp(ii))^2))*((t
emp(ii)-temp(ii-1))/(dz)))] + [0;(-g/(3*vm(temp(ii))))];
dk = B;
end
function dj = viewfactor(r2,d0,dz,r)

D1 = d0/r2;
Y1 = dz/r2;
R1 = r/r2;
function de = epsilon(ep,R1)
Aep = (ep^2)+(R1^2)-1;
Bep = (ep^2)-(R1^2)+1;
F1 = Bep/(8*R1*ep);
```

```
F2 = acos(Aep/Bep);
F3 = ((((((Aep+2)^2)/(R1^2))-4)^0.5)/(2*ep));
F4 = acos(Aep*R1/Bep);
F5 = Aep*asin(R1)/(2*ep*R1);

Fep = F1+((F2-((F3*F4))-F5)/(2*pi));
de = Fep;
end
Ff = (2*((Y1+D1)*epsilon((Y1+D1),R1)/Y1))-(D1*epsilon(D1,R1)/Y1) -
((Y1+Y1+D1)*epsilon((Y1+Y1+D1),R1)/Y1);
Fp = r*Ff/r2;
dj = Fp;


end

function dg = adjacent(r,r2,dz)
nr1 = r/dz;
nr2 = r2/dz;
Ar1 = nr2+nr1;
Ar2 = nr2-nr1;

vf1 = ((nr2^2)-(nr1^2)-1)/2;
vf2 = acos(nr1/nr2);
vf3 = (pi*nr1)-(pi*Ar1*Ar2/2);
vf4 = ((nr2^2)-(nr1^2))^0.5;
vf5 = 2*nr1*atan(vf4);
vf6 = (1+(Ar1^2));
vf7 = (1+(Ar2^2));
vf8 = atan(((vf6*Ar2)/(vf7*Ar1))^0.5);
vf9 = ((vf6*vf7)^0.5)*vf8;

Vf = ((vf1*vf2)+vf3-vf5+vf9)/(pi*nr2);

dg = Vf;
end

function dq = radiation(e2,r2,e1,r,sig,Tw,temp,vff)

den1 = (1-e2)/r2;
den2 = (1-e1)/r;
den3  = 1/(r2*vff);
den = r*(den1+den2+den3)
qr= sig*(((Tw+273)^2)+((temp+273)^2))*(Tw+temp+273+273)./den;
dq = qr;

end
```